

## Toward large-scale fine resolution DEM landslide simulations: periodic granular box for efficient modeling of excavatable slope

Jian Chen <sup>a,\*</sup>, Mikito Furuichi <sup>a</sup>, Daisuke Nishiura <sup>a</sup>

<sup>a</sup> Center for Mathematical Science and Advanced Technology, Japan Agency for Marine-Earth Science and Technology, 3173-25 Showa-machi, Kanazawa-ku, Yokohama, Kanagawa 236-0001, Japan



### ARTICLE INFO

**Keywords:**

Landslide simulation  
Discrete element method (DEM)  
Periodic granular box  
Numerical triaxial test  
Excavatable slope model

### ABSTRACT

Understanding landslide hazards and developing mitigation measures is critical to protecting lives and property. The Discrete Element Method (DEM) has demonstrated its ability to simulate landslides and estimate impact forces on mitigation structures. Such simulations often model slope surfaces as bedrock on which a fixed amount of earth mass is released and slides. Mass entrainment due to local failure of an excavatable slope surface is rarely modeled with sufficient resolution. Fine-resolution modeling of an excavatable slope for simulation is necessary and non-trivial to improve DEM simulations of large-scale landslides. In this study, we present a method based on Periodic Granular (PG) boxes for efficient modeling of excavatable slopes. A PG box is a packing of particles in a quasi-static state inside a virtual unit box, where the periodic boundary conditions are satisfied at the box surfaces. The procedures used to construct a PG box are presented. The quality of PG boxes is analyzed both at the particle contact scale and at the laboratory specimen scale by measuring contact orientation statistics and by performing numerical triaxial tests. As a demonstration, a centimeter resolution slope model constructed using the PG box-based method is presented using topographic data for the Aso Bridge landslide. In addition, landslide simulations to verify the excavation effect were performed on sub-meter resolution slope models. Our simulations show that landscape shape and particle size have a direct effect on the movement and deposition of earth masses. This highlights the need for detailed 3D terrain modeling and further study of particle size effects. By constructing the first excavatable DEM slope model with billions of centimeter-sized particles, this study can be considered a solid step toward fine-resolution DEM simulations of large-scale landslides, which can contribute to both scientific understanding and engineering countermeasures to mitigate the catastrophic consequences of large-scale landslides.

### 1. Introduction

Landslides are the geologic processes of downslope movement of earth masses, such as rocks and soils that are triggered by a variety of factors, including earthquakes, intense precipitation, and human activities [(Highland & Bobrowsky, 2008)]. Such movements can occur in a short time or spread over a long period with varying speeds. Landslides, especially fast-moving ones, can cause direct damage to infrastructure and result in many killed and injured. Large-scale landslides often have lasting socioeconomic impacts: the Aso Bridge landslide [(Dang, et al., 2016; Song, et al., 2019; Doi, et al., 2019)], see Fig. 1(a), is a typical example where it took 4–5 years to rebuild the damaged bridge, railroad, and highway. As a result, landslides are considered to be one of the most costly natural disasters in the world [(Dilley, et al., 2005)]. To

improve the understanding of the complex motion of landslides and to mitigate their catastrophic and life-threatening consequences, landslides have attracted great attention and continuous efforts from researchers from many disciplines with a wide range of research priorities and approaches: see, e.g., the review for co-seismic landslides [(Wasowski, et al., 2011; Jibson, 2011)] and the references therein. In this study, we limit ourselves to physics-based numerical simulations of landslides.

Physics-based numerical simulations are versatile tools for studying the different stages of landslides from initiation to post failure, see, e.g., [(Crosta, et al., 2005; Bui, et al., 2008; Wang & Sassa, 2010; Huang, et al., 2011; Soga, et al., 2016; Hung, et al., 2019)]. A physics-based landslide simulation solves the equations of motion for the earth masses involved. There are two main types of approaches, one based on continuum mechanics and the other based on discrete mechanics. In a

\* Corresponding author.

E-mail addresses: [jchen@jamstec.go.jp](mailto:jchen@jamstec.go.jp) (J. Chen), [m-furuic@jamstec.go.jp](mailto:m-furuic@jamstec.go.jp) (M. Furuichi), [nishiura@jamstec.go.jp](mailto:nishiura@jamstec.go.jp) (D. Nishiura).

continuum mechanics approach, the earth masses are modeled as continua and their behavior is described by the governing equations. Given a constitutive law and appropriate boundary and initial conditions, the governing equations become a closed system of partial differential equations (PDEs) that can be solved by various numerical methods. Mesh-based numerical methods for PDEs, such as the finite element method (FEM), the finite volume method (FVM), and the finite difference method (FDM), can be used, see, e.g., Crosta et al. (2005), Liu et al. (2019), and Wang & Sassa (2010), respectively. For flow-like landslides and for the post failure processes, mesh-free techniques such as Smoothed Particle Hydrodynamics (SPH), Material Point Method (MPM) are better suited to handle the time-varying free surfaces, see e.g., SPH simulations of landslides [(Huang, et al., 2011; Dai, et al., 2016; Bao, et al., 2020; Morikawa & Asai, 2022)] and MPM simulations of landslides [(Soga, et al., 2016; Troncone, et al., 2022)].

Recently, the Discrete Element Method (DEM) has gained momentum in landslide simulation [(Hung, et al., 2019; Peng, et al., 2019; Lai, et al., 2022; Mreyen, et al., 2022)], especially due to its ability to estimate the impact forces of soils (rocks) on structures [(Zhang, et al., 2021; Zhang & Huang, 2022)]. DEM is a discrete mechanics approach in which the motion of a single particle is resolved from its interaction with neighbors [(Cundall & Strack, 1979; Matutti & Chen, 2014)]. Unlike continuum-mechanics based approaches, there is no underlying assumption of continuity and smoothness of the field functions. Instead, DEM solves a system of ordinary differential equations (ODEs), which are generally much simpler than PDEs. In a DEM landslide simulation, both soils (rocks) and engineering structures can be simply modeled as a collection of DEM particles, and the impact force on the structures can be obtained directly from the particle interactions. This feature is particularly useful for evaluating the performance of mitigation structures, see for example, Zhang et al. (2021) and Zhang & Huang (2022).

A critical limitation of current DEM simulations of large-scale landslides is the model resolution, or simply the number of particles used to

model the slope. The concept of DEM is to model each individual grain as a particle [(Cundall & Strack, 1979; Matutti & Chen, 2014)]. However, in most DEM landslide simulations, especially those that targeting real slope topography, the resolution is coarse: a DEM particle has a diameter of meters or larger, as in Hung et al. (2019), Lai et al. (2022), and Mreyen et al. (2022), for example. Such a particle size is much larger than a typical laboratory specimen for measuring soil mechanical properties, and larger than state-of-the-art sub-meter topography data. To achieve a fine resolution landslide simulation, a reasonable and realistic particle size should be at least smaller than the scale of laboratory soil specimens or fine-resolution topographic data. Such a fine resolution would result in millions or even billions of DEM particles for simulating landslides on real slopes, such as the Aso Bridge landslide shown in Fig. 1(a). To avoid modeling of the slope directly, slope surfaces are often considered as motionless bedrock and modeled by fixed boundary particles, which are different from the DEM particles for the free earth masses in the literature, see, e.g., [(Zhang, et al., 2021; Zhang & Huang, 2022; Hung, et al., 2019; Lai, et al., 2022)]. A fixed surface excludes the consideration of excavatable slopes during sliding, where the excavation and soil entrainment is an important factor in determining the total volume and runout distance of a landslide [(Iverson, et al., 2011; Iverson & Ouyang, 2015; Berzi, et al., 2020; Pudasaini & Krautblatter, 2021; Liu, et al., 2019)]. An excavatable surface should be considered for DEM landslide simulations (Zhu, et al., 2023) with sufficient fine resolution, although it requires more computational resources and coding skills.

Billion-particle DEM simulations are feasible and have been demonstrated for numerical sandbox experiments to study structural geology [(Furuichi, et al., 2017; Furuichi, et al., 2018)] using high performance computing (HPC). However, compared to the rectangular prism geometry in a sandbox simulation, the complex slope topography, see, e.g., Fig. 1(b), poses a new challenge for large-scale DEM landslide simulations: how to efficiently construct the slope model for landslide

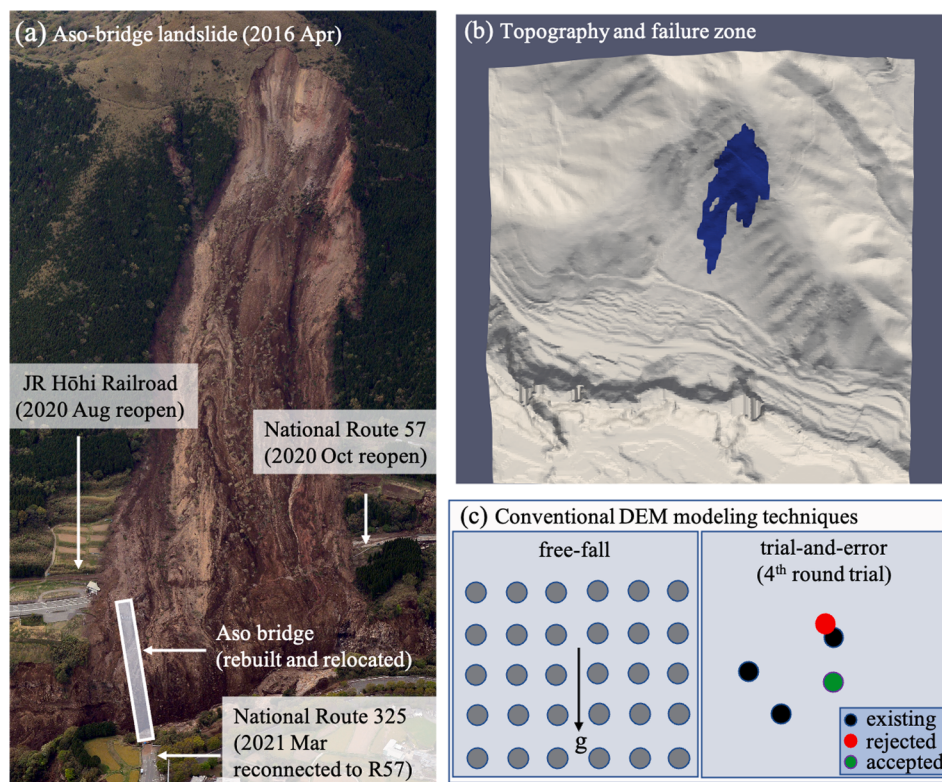


**Fig. 1.** (a) The Aso Bridge landslide caused by the 2016 Kumamoto earthquake has had lasting socioeconomic impacts. (b) The main failure zone (in blue) of the Aso Bridge landslide as determined from meter-scale topographic data; (c) The free-fall and trial-and-error techniques commonly used for DEM modeling are not applicable or extremely difficult to model actual large-scale slopes as in (b) for landslide simulations.

simulations. Conventional techniques such as free-fall, trial-and-error, drop-and-roll, and graph-based methods are widely used to generate DEM models [(Visscher & Bolsterli, 1972; Liu & Thompson, 2000; Campello & Cassares, 2016; Bonneau, et al., 2021; Jerier, et al., 2010)]. The free-all and the trial-and-error techniques, the two most common, are shown in Fig. 1 (c). In the free-all method, the particles are first placed over a container of the desired geometry and allowed to fall by gravity. A model is obtained when the particles reach static equilibrium. In the trial-and-error method, particles are inserted randomly and sequentially into a container, and each new insertion attempt must pass a test against the existing particles to avoid overlap. For small-scale models, these conventional techniques are preferable due to their simplicity and ease of use. With appropriate preprocessing, they can be adapted to generate small-scale models with complex boundaries. For large-scale models with millions or even billions of particles that require parallel processing, it is difficult to apply these conventional modeling techniques to construct models with complex geometry, especially for a slope with an excavatable surface as shown in Fig. 1(a-b). Even if it is possible to use these techniques with extensive and complicated preprocessing, the cost of modeling would increase both in terms of code implementation and computation. A more efficient and flexible modeling technique is needed to construct large DEM models with complex geometry.

A novel modeling technique for constructing large-scale slope models for landslide simulation is presented in this study. It is based on Periodic Granular (PG) boxes and is capable of constructing complex DEM models, such as slope models from topographic data. A PG box is a packing of particles whose boundary surfaces satisfy periodic boundary conditions. We generate PG boxes by iterative procedures and quantify the quality of the PG boxes in terms of fabric properties and mechanical properties measured from numerical triaxial tests. The use of the periodic boundary conditions in the literature is often aimed at reducing the number of particles in DEM simulations, e.g., [(Cundall, 1988; Thornton, 2000; Cui, et al., 2007; Yang, et al., 2014)]. In this study, periodic boundary conditions are used to prepare PG boxes as primitive building blocks with a controlled volume fraction and measured fabric and mechanical properties. To construct large complex models, these primitive PG boxes are rescaled and connected to fill a spatial domain. They are then trimmed to fit a simulation model of interest, which may have complex boundaries. As a demonstration, slope models are constructed from the digital elevation model data of the Aso Bridge landslide. A fine-resolution slope composed of 6.5 billion particles with a maximum radius of 5 cm is presented, and the computational resources required by the PG box-based and the adapted free-fall techniques are compared. A test simulation is performed on a coarser slope model of 8 million particles with a maximum radius of 5 decimeters, from which excavation and soil entrainment can be seen.

This study presents one of the first large-scale DEM landslide models with excavatable surfaces composed of centimeter-sized particles. It can be considered as a solid step towards large-scale DEM landslide simulations. DEM simulations with such fine-resolution models are expected to contribute to both the scientific understanding of landslides and the engineering mitigation of their catastrophic consequences. Furthermore, the PG box-based modeling method is not limited to landslide simulations. It can be applied to large-scale DEM simulations in many other fields to investigate problems with complicated boundary geometry.

The rest of the paper is organized as follows. In Sec. 2, we briefly explain the DEM method and the particle interaction models, the PG box-based modeling technique, and an iterative procedure for constructing primitive PG boxes. In Sec. 3, we analyze the fabric and mechanical properties of PG boxes. The mechanical properties are measured by numerical triaxial tests. A demonstration of a fine slope model constructed using the PG box method for the Aso Bridge landslide is presented in Sec. 4, along with a test landslide simulation. The advantages and limitations are discussed in Sec. 5, followed by a summary in the last section.

## 2. Methodology

### 2.1. Discrete element method

In a DEM simulation, the Newton–Euler equations of motion are solved for each particle [(Cundall & Strack, 1979; Matuttis & Chen, 2014)],

$$m\ddot{\mathbf{x}} = \sum \mathbf{F}, \quad (1)$$

$$\mathbf{J}\dot{\boldsymbol{\omega}} = \sum \mathbf{T}, \quad (2)$$

where  $m$  and  $\mathbf{J}$  are the mass and moment of inertia of a particle,  $\mathbf{x}$  and  $\boldsymbol{\omega}$  are the center of mass and the angular velocity,  $\mathbf{F}$  and  $\mathbf{T}$  are the forces and torques acting on the particle and the summation  $\sum$  operation is over all the particle interactions plus any external field force, e.g., gravity. The basic interaction models for DEM particles include a combination of the spring and dashpot model and a frictional slider model. For two particles in contact, the forces from a nonlinear spring-dashpot model, the Hertz–Mindlin model [(Hertz, 1881; Mindlin, 1949)] and the Coulomb friction model in the normal ( $\mathbf{n}$ ) and tangent ( $\mathbf{t}$ ) directions, are as follows:

$$\mathbf{F}_{sd}^{n,t} = -K_{ij}^{n,t} \delta_{ij}^{n,t} - \eta_{ij}^{n,t} v_{ij}^{n,t}, \quad (3)$$

$$\mathbf{F}_t^t = -\min(|\mathbf{F}_{sd}^t|, \mu |\mathbf{F}_{sd}^n|) \mathbf{t}, \quad (4)$$

with

$$\mathbf{n} = \frac{\mathbf{x}_j - \mathbf{x}_i}{|\mathbf{x}_j - \mathbf{x}_i|}, \quad (5)$$

$$\mathbf{v}_{ij}^n = (\mathbf{v}_i - \mathbf{v}_j)(\mathbf{n} \otimes \mathbf{n}), \quad (6)$$

$$\mathbf{v}_{ij}^t = (\mathbf{v}_i - \mathbf{v}_j) - \mathbf{v}_{ij}^n, \quad (7)$$

$$\mathbf{t} = \left( \mathbf{v}_{ij}^t + (r_i \boldsymbol{\omega}_i + r_j \boldsymbol{\omega}_j) \times \mathbf{n} \right) / |\mathbf{v}_{ij}^t + (r_i \boldsymbol{\omega}_i + r_j \boldsymbol{\omega}_j) \times \mathbf{n}|, \quad (8)$$

$$K_{ij}^n = \frac{2E}{3(1-\nu^2)} \sqrt{\frac{r_i r_j}{r_i + r_j} |\delta_{ij}^n|}, \quad (9)$$

$$K_{ij}^t = \frac{3(1-\nu)}{2-\nu} K_{ij}^n, \quad (10)$$

$$\eta_{ij} = \frac{1}{2.2} \ln \left( \frac{2}{e} - 1 \right) \sqrt{\frac{m_i m_j}{m_i + m_j} K_{ij}}, \quad (11)$$

where  $\delta = (\delta_{ij}^n \mathbf{n}, \delta_{ij}^t \mathbf{t})$  is the relative displacement vector between two interacting particles,  $\otimes$  the tensor product,  $r_i$  and  $r_j$  the radii of particle  $i$  and particle  $j$ ,  $\mu$  the friction coefficient,  $E$  the Young's modulus,  $\nu$  the Poisson's ratio,  $e$  the coefficient of restitution, and  $\eta_{ij}$  the damping coefficient [(Chen, et al., 2020; Chen, et al., 2021; Chen, et al., 2022)]. The normal displacement  $\delta_{ij}^n$  is given by

$$\delta_{ij}^n = r_i + r_j - |\mathbf{x}_j - \mathbf{x}_i| - \delta_{ij}^{n0}, \quad (12)$$

where  $\delta_{ij}^{n0} = 0$  for common use and a finite value of  $\delta_{ij}^{n0}$  to offset initial overlap for modeling a stress-free initial condition [(Jerier, et al., 2011; Scholtès & Donzé, 2013)]. The tangential displacement  $\delta_{ij}^t$  is calculated incrementally for a contact

$$\delta_{ij}^t(t) = \sum \mathbf{v}_{ij}^t \Delta t, \quad (13)$$

where  $\Delta t$  is the time step in DEM simulations.

For landslide simulations, it is important to consider the cohesive behavior of soils. Without a cohesive force, it is impossible to construct a

stable packing of particles to model a slope with an excavatable surface. In this study, we implement a bonding model for cohesive forces [(Furuichi, et al., 2023)], as a complement for the above contact force models. The (maximal) normal and tangential bonding forces are as follows:

$$\mathbf{F}_b^n = P_b \pi \left( \frac{2r_i r_j}{r_i + r_j} \right)^2 \mathbf{n}, \quad (14)$$

$$\mathbf{F}_b^t = -(\mu |F_{sd}^n| + \mu_b |F_b^n|) \mathbf{t}, \quad (15)$$

where  $(P_b, \mu_b)$  are the bond parameters, one as the strength parameter and the other as the ratio parameter, respectively. These two parameters can be calibrated [(Scholtès & Donzé, 2013)] from the cohesion and angle of internal friction ( $c, \phi$ ) parameters of the Mohr–Coulomb failure envelope,

$$\tau_m = c + \sigma_m (\tan \phi), \quad (16)$$

where  $\tau_m$  is the shear strength of a soil specimen and  $\sigma_m$  the applied normal stress.

The total normal and tangential forces, as a combination of the contact and bonding models, in Eqs. (3–4) and in Eqs. (14–15), are summarized as follows:

$$\mathbf{F}^n = \begin{cases} \mathbf{F}_{sd}^n & \delta_{ij}^n \geq 0 \text{ or } (\delta_{ij}^n < 0 \text{ and } B_{ij} = 1 \text{ and } |F_{sd}^n| \leq |F_b^n|), \\ 2\mathbf{F}_b^n - \mathbf{F}_{sd}^n & \delta_{ij}^n < 0 \text{ and } B_{ij} = 1 \text{ and } |F_{sd}^n| > |F_b^n|, \\ \mathbf{0} & \text{other,} \end{cases} \quad (17)$$

and

$$\mathbf{F}^t = \begin{cases} \mathbf{F}_f^t & \delta_{ij}^t \geq 0 \text{ and } B_{ij} = 0, \\ \mathbf{F}_{sd}^t & B_{ij} = 1, \\ \mathbf{0} & \text{other,} \end{cases} \quad (18)$$

where  $B_{ij}$  is the bond state, with 1 and 0 representing active and inactive bonds, respectively. Debonding occurs when an initially active bond between a pair of neighboring particles becomes inactive. This happens when the attractive normal force during particle separation

$$|F_{sd}^n| \geq 2|F_b^n|, \quad (19)$$

or when the tangential force

$$|F_{sd}^t| > |F_b^t|, \quad (20)$$

for a bonded particle pair, where  $F_{(\bullet)}^n = F_{(\bullet)}^n \cdot \mathbf{n}$  and  $F_{(\bullet)}^t = F_{(\bullet)}^t \cdot \mathbf{t}$ , respectively. In this study, once an initially bonded pair is debonded, it is not recovered. Ignoring damping ( $\eta = 0$ ) for simplicity, the force–displacement relationships in Eqs. (17–18) are shown in Fig. 2. This combination of bonding and contact force models is inspired by Scholtès & Donzé (2013) to account for the strength due to grain interlocking, replacing their linear springs with the contact-mechanics-based Hertz–Mindlin model.

The force models are implemented in the DEM-based Parallel muLtiPhySics simulator (DEPTH), a DEM code that takes advantage of hybrid MPI and OpenMP parallelization [(Nishiura & Sakaguchi, 2011; Nishiura, et al., 2015; Furuichi & Nishiura, 2017)], enabling large-scale DEM simulations with billions of particles [(Furuichi, et al., 2017; Furuichi, et al., 2018)].

## 2.2. Periodic granular box and “glue-and-trim” modeling technique

A PG box is a box of granular particles that satisfy the periodic boundary conditions on its three pairs of opposite faces. Suppose that the box is of size  $L$ , aligned with the Cartesian coordinate system. Taking the  $x$ -direction for example, periodicity means that for one particle located at  $x$ , there are identical particles located at  $x+nL$  ( $n = 1, 2, \dots$ ). Therefore, satisfying the periodic boundary condition for the pair of opposite faces along the  $x$ -direction requires that the particles located near to the surface at  $x = 0^+$  are neighbors of the particles located near to the surface at  $x = L^-$  [(Cundall, 1988)]. In DEM simulations, see e.g. [(Yang, et al., 2014; Cui, et al., 2007; Thornton, 2000)], periodic boundary conditions have been adopted to reduce the size of the model: the size of the direction with (assumed) periodicity is limited to  $L$  instead of its real size, which is much larger than  $L$ .

By exploiting periodic boundary conditions, primitive PG boxes can be seamlessly connected to form large packings at low computational cost. Although there is a preprocessing cost for constructing PG boxes, once a primitive PG box is prepared, e.g., see Fig. 3(a), a regular packing of arbitrary size can be obtained by simply “gluing” the primitive boxes to a regular grid, e.g., see Fig. 3(b). From the regular packing, it is easy to obtain a DEM model of any desired shape by “trimming” the particles outside the model boundary, or by treating them as boundary particles, e.g., see Fig. 3(c) top and bottom, respectively. For better visibility, the particles in Fig. 3 are much larger than those used in practice, e.g., the cylindrical specimens used for the triaxial tests in Sec. 3.2 are made with

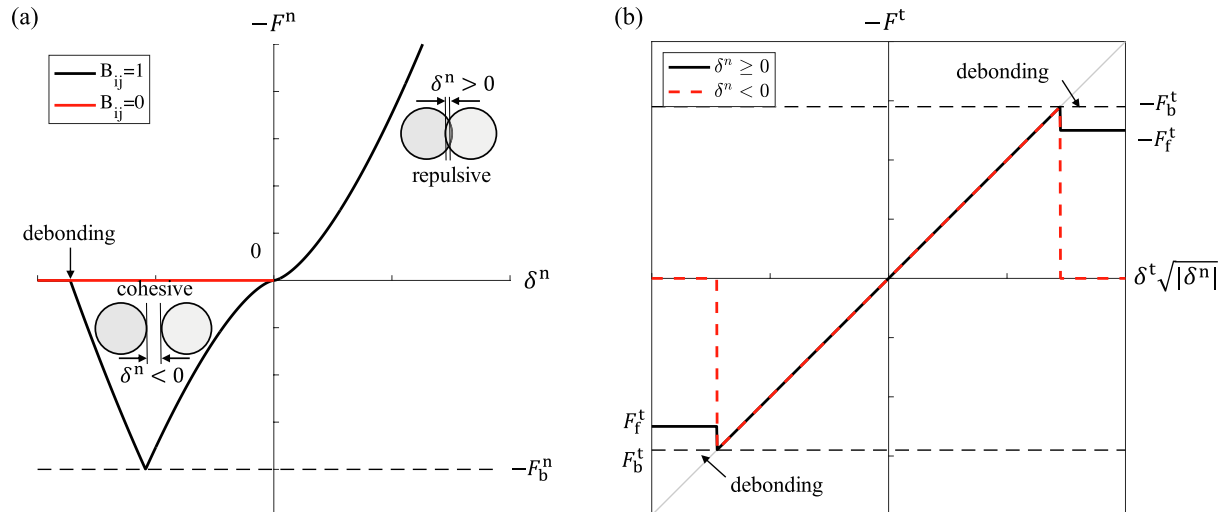


**Fig. 2.** Bonding forces in the (a) normal and (b) tangential directions, where  $F_{(\bullet)}^n = F_{(\bullet)}^n \cdot \mathbf{n}$  and  $F_{(\bullet)}^t = F_{(\bullet)}^t \cdot \mathbf{t}$ .

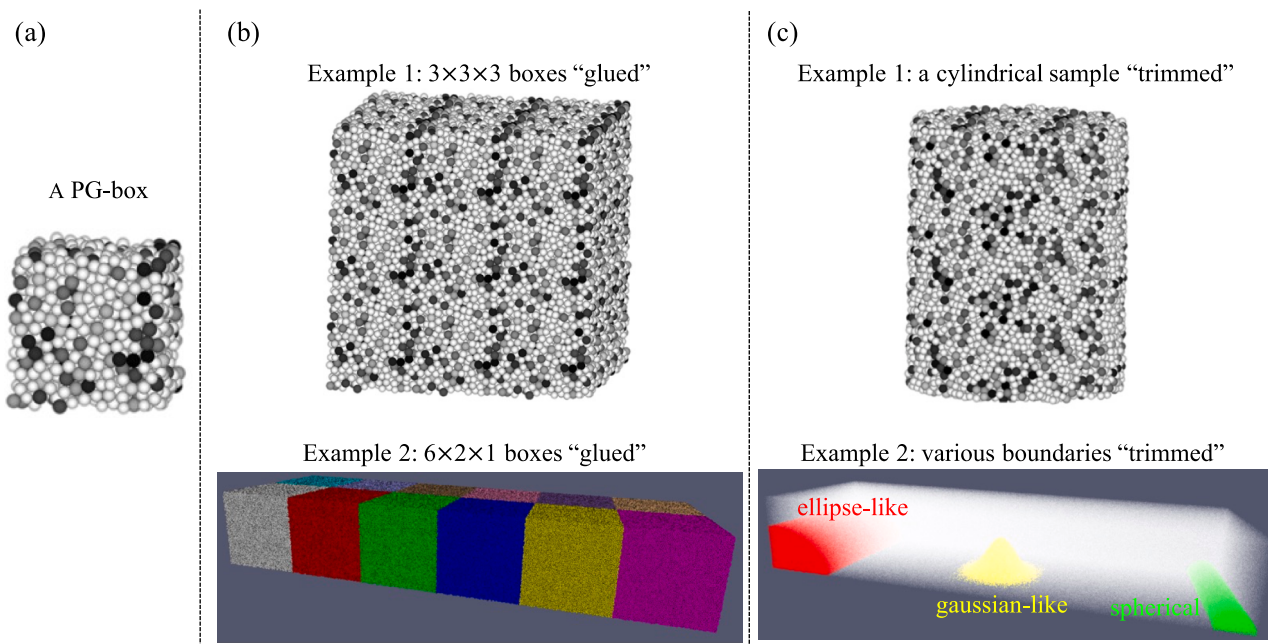


**Fig. 3.** Schematic of the PG box-based modeling method: (a) Example of a primitive PG box; (b) PG boxes “glued” to a regular grid covering a model to be constructed; (c) DEM models created by trimming the regular packings in (b). Particles outside the desired model boundary can either be removed to form a single DEM model (top) or retained as boundary particles to model multiple boundaries of different types (bottom).

much finer particles. The main cost of constructing a large-scale DEM model (of arbitrary shape) using this glue-and-trim scheme is the preparation of the PG boxes. This cost is negligible compared to conventional modeling techniques such as free-fall and trial-and-error to directly construct large-scale models.

### 2.3. Iterative method for constructing a PG box

The application of a periodic boundary condition is a common model-size reduction technique in DEM simulations. A periodic boundary condition is often imposed in one or two directions because a reference (fixed) boundary is needed to avoid rigid-body translation of the entire packing when an external load is applied. Because of this rigid-body translation, it is difficult to obtain a converged solution by imposing periodic boundary conditions in all three dimensions, similar to the difficulty of solving a pure Neumann boundary condition for the

Poisson equation. To construct a PG box that satisfies periodic boundary conditions in its three pairs of opposite faces, we adopt a method characterized by an interactive procedure. In this method, four main steps are involved to generate a cubic PG box of side length  $L$ . For simplicity, we describe the method for monodisperse particles with radius  $r_i = r$ , which can be extended to polydisperse particles. A schematic summary of the construction of a PG box is shown in Fig. 4.

The first step is to create a rectangular box of particles, e.g., using the free-fall technique. The particles are initialized inside a rectangular domain  $\Omega^*$  with side lengths  $L \times L \times L^*$  (where  $L^* > L$ ) and fall into the box under gravity along the  $z$ -direction. Periodic boundary conditions are applied to the side walls along the  $x$ - and  $y$ -directions, i.e.,  $(\partial\Omega^*)_{x=0} = (\partial\Omega^*)_{x=L}$  and  $(\partial\Omega^*)_{y=0} = (\partial\Omega^*)_{y=L}$ . The fixed wall condition is applied at the bottom  $(\partial\Omega^*)_{z=0}$ . Particles subjected to this free-fall process are assigned with randomly perturbed velocities to initial crystallization during sedimentation. To minimize crystallization during

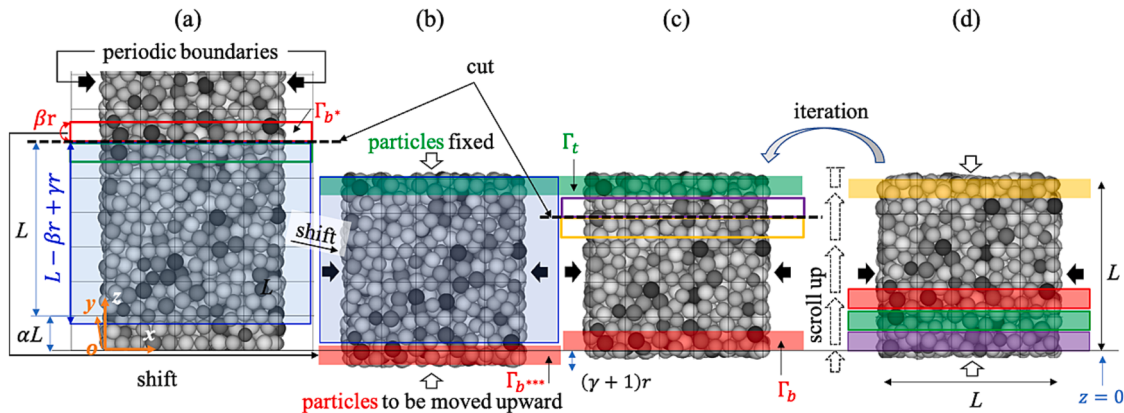


**Fig. 4.** Main steps to create a PG box: (a) Create a rectangular box of particles with periodic boundary conditions imposed on the lateral directions; (b) Create boundary particles that satisfy the boundary condition in the  $z$ -direction by a “cut-and-shift” operation: cut the box with a plane indicated by the dashed line in (a); shift the particles in the blue box down by  $aL$  to  $z = 0$ ; shift a layer of particles in the red box ( $\Gamma_b$ ) to the region  $\Gamma_{b^{***}}$  (shaded in red) below  $z = 0$ . (c) Compress  $\Gamma_{b^{***}}$  to the position of  $\Gamma_b$ , making the PG box cubic with periodic boundary conditions satisfied in all three pairs of boundary surfaces. (d) Homogenize the particle distribution in the PG box by iteration: a new cut plane is selected and the cut-and -paste operation followed by compression is performed repeatedly.

loading, variation in size [(Oger et al., 2007)] or shape [(Krengel et al., 2023)] are effective means in DEM simulations. Here we use mono-dispersed particles to investigate the effect of particle size on PG box properties. For landslide simulations, particle radii were uniformly distributed within  $[0.82, 1] \cdot r_{\max}$ . In terms of particle volume, the smallest particle was only 55% of the largest particle. After the free-fall process, a rectangular box of particles is sedimented as shown in Fig. 4(a). The height of the domain  $L^*$  is chosen to be large enough to obtain a sedimentation height greater than  $(1.0 + \alpha)L$ , where  $\alpha$  is an arbitrary coefficient satisfying  $\alpha L \gg r$ , e.g.,  $\alpha = 0.25$  in this study. This extra height  $\alpha L$  allows operations in the next step to minimize the influence of the fixed bottom wall at  $z = 0$  during the free-fall process. The sedimented particles near the surfaces of the rectangular box in the  $x$ - and  $y$ -directions automatically satisfy the periodic boundary conditions.

The second step is to create boundary particles that satisfy the periodic boundary condition in the  $z$ -direction. This is achieved by a “cut-and-shift” operation that exploits the fact that the particles located above and below any cut plane can satisfy the periodic boundary condition. Therefore, we choose a cut plane orthogonal to the  $z$ -axis, e.g., a plane at  $z = (1.0 + \alpha)L$ , as shown in Fig. 4(a). Denote the center of mass of a particle  $i$  as  $\mathbf{x}_i = (x_i, y_i, z_i)$ . The particles within the upper region  $\Gamma_{b^*}$ ,  $\{\mathbf{x}_i \in \Gamma_{b^*} : (1 + \alpha)L \leq z_i < (1 + \alpha)L + \beta r\}$ , see the red box in Fig. 4(a), are sliced and stored in a buffer. Here,  $\beta$  is a parameter to adjust the thickness of the sliced layer (e.g.,  $\beta = 3$ ). To avoid the influence of the fixed boundary at  $z = 0$  in the first step, we select particles inside the region  $\Omega^{**}$  where  $\{\mathbf{x}_i \in \Omega^{**} : \alpha L + (\beta - \gamma)r \leq z_i < (1 + \alpha)L\}$ , the blue box in Fig. 4(b), and remove particles outside the region. In total, the particles within a volume of  $(L + \gamma r) \times L \times L$  from the initial sample created in Step 1 have been selected from the initial sample to create a PG box of volume  $L \times L \times L$ . The parameter  $\gamma$  is used to fine-tune the solid volume fraction from  $\psi_i$  of the initial sample to a target value  $\psi_t$  for the PG box:  $(L + \gamma r)\psi_i \approx L\psi_t$ . Note that the final PG box is denser than the initial sample ( $\psi_t > \psi_i$  and  $\gamma > 0$ ). To obtain loose PG boxes, a loose initial sample should be prepared, e.g., by adjusting the sedimentation friction. The remaining particles in  $\Omega^{**}$  are translated down along the  $z$ -direction by  $\alpha L$  to their new positions  $\{\mathbf{x}_i \in \Omega^{***} : (\beta - \gamma)r \leq z_i < L\}$ . Then, the buffered particles in  $\Gamma_{b^*}$  from the upper region of the cut plane are moved to the bottom of  $\Omega^{***}$  as its new bottom layer  $\Gamma_{b^{***}} \{-(\gamma + 1)r \leq z < (\beta - \gamma - 1)r\}$ , see Fig. 4(b). Note that a safety distance  $r$  is introduced layer to avoid possible initial overlap between the layers  $\Gamma_{b^{***}}$  and  $\Omega^{***}$ , resulting in a total height of the configuration as  $L + (\gamma + 1)r$ .

Then, in the third step, the particles of the bottom layer  $\Gamma_{b^{***}}$  indicated by the red area in Fig. 4(b) are slowly compressed upwards. The top layer of particles  $\{\mathbf{x}_i \in \Gamma_t : L - \beta r \leq z_i < L\}$  in the green area of Fig. 4(b) is fixed, and periodic boundary conditions are applied to the side-walls in the  $x$ - and  $y$ -directions. When  $\Gamma_{b^{***}}$  reaches its final position as  $\Gamma_b \{ \Gamma_b : 0 \leq z < \beta r \}$ , see Fig. 4(c), a PG box of size  $L \times L \times L$  is obtained with boundary particles satisfying periodic boundary conditions in all its opposite faces. This operation can lead to local dense zones in the sample, requiring a subsequent homogenization step.

Finally, in the fourth step, the PG box is iteratively homogenized. Note that in the third step, the packing conditions for the particles in the bottom and top layers, i.e.,  $\mathbf{x}_i \in (\Gamma_t \cup \Gamma_b)$ , are different from those of the particles in the middle layer far from the loading region. To homogenize the particle distribution throughout the whole box, the cut-paste operation in step 2 followed by the compression in step 3 is repeated iteratively, as shown in Fig. 4(c) and (d). In this iterative procedure, we first select a new cut plane (e.g.,  $z_{\text{new}} = 0.8L$ ) as the new boundary in the  $z$ -direction. The region below  $z_{\text{new}}$ , see the yellow box in Fig. 4(c) and (d), becomes the new top layer  $\Gamma_t$ . Then, the region above  $z_{\text{new}}$ , see the yellow box in Fig. 4(c) and (d), is moved to become the new  $\Gamma_{b^*}$  and compressed upward to become the new bottom layer  $\Gamma_b$ . Meanwhile, the old top and bottom layers, the red and green boxes in Fig. 4(c) and (d), are moved up. This process can be iterated until all particles are scrolled and

homogenized, or until some of the observed quantities, such as total particle overlap, are saturated.

Note that the above method is not the only one for constructing a PG box. Other methods, such as the servo-control method introduced by Cundall (1988) can be extended. Instead of controlling the mean stress within the box, it may be necessary to control the three principal stresses to achieve an isotropic loading. Once a PG box is available, the PG box-based modeling technique in Sec 2.2 can be used to construct more complex DEM models for simulation.

### 3. Quality analysis of PG box

In this section, we will analyze the quality of PG boxes in terms of their fabric (internal structure) and mechanical properties. Since the number of particles that make up a PG box is a primary property, we will study how changing the number of particles affects the quality of PG boxes.

#### 3.1. Fabric properties

To evaluate the fabric properties, we created PG boxes of the same size with the DEM parameters listed in Table 1. PG boxes with different levels of resolution were considered for a unit cubic domain of side length  $L = 1.0$  m. “Fine” and “coarse” resolution PG boxes refer to PG boxes composed of smaller and larger particles, respectively. A fine unit PG box consists of more particles than a coarse unit PG box, and is therefore more computationally expensive to create. We created unit-PG boxes of 5 different resolutions, from the finest to the coarsest, with particle sizes of  $r = 0.005, 0.01, 0.03, 0.06$ , and  $0.09$  m, respectively. For each resolution, we created unit PG boxes under frictionless and frictional conditions, i.e.,  $\mu = 0.0$  and  $\mu = 0.4$ , respectively. Note that the particle density is chosen to be the same as that of water, so that the created unit PG boxes can be easily rescaled to different types of materials based on their specific gravity.

The combination of resolution level and friction condition resulted in 10 different unit PG boxes. We assigned these PG boxes labels reflecting their main characteristics as “PL#” and “PF#”, where PL and PF refer to PG boxes made under frictionless and frictional conditions, and # = 0 ~ 4 for their resolution level. The smaller the #, the finer the PG box. The volume fractions were adjusted to about 0.64 by tuning the parameter  $\gamma$  in the second step of the PG box construction described in Sec. 2.3, which essentially compressed the relatively loose initial packings to the same dense states. Using a fixed volume fraction allows to exclude the influence of packing density when check the influence of the PG box resolutions. The iterations in the fourth step were performed until the total overlap of a PG box was saturated and a quasi-static state was reached. As shown in Table 2, our method successfully yielded PG boxes with well-controlled macroscopic and microscopic fabric properties, in terms of volume fraction and mean coordination number (i.e., number of neighboring particles in contact), respectively. Note that here a PG box was made of identical particles to investigate the convergence of the macroscopic properties with respect to particle size, i.e., model resolution level. For practical applications, one should model soils with size distribution, for which the PG construction method presented in Section 2 is applicable. For the trial simulations of the Aso-Bridge landslide in

**Table 1**  
DEM parameters used to create a periodic granular (PG) box.

Particle density $\rho$	1,000 kg/m <sup>3</sup>
Young's modulus $E$	$1 \times 10^8$ Pa
Poisson's ratio $\nu$	0.2
Coefficient of restriction $e$	0.2
Particle radius	0.005, 0.01, 0.03, 0.06, and 0.09 m
Coefficient of friction $\mu$	0.0 and 0.4

**Table 2**

Summary of the microstructural and fabric properties of unit PG boxes of different resolutions generated under frictionless and frictional conditions. *RSD* and *Kurt* refer to the relative standard deviation and the kurtosis of  $\{\delta^n\}$ , a set of mean values of the normalized overlap vector which are averaged over 18 consecutive polar angle intervals between  $[0, 90^\circ]$ .

Friction condition	Box label	Resolution level	Radius r [m]	# of particles	Volume fraction	Coordination number	(RSD, Kurt) of $\{\delta_i^n\}$
frictionless ( $\mu = 0.0$ )	PL0	0 (finest)	0.005	1,222,346	0.640	6.086	(0.95%, -)
	PL1	1	0.01	152,799	0.640	6.116	(1.27%, -)
	PL2	2	0.03	5,660	0.640	6.271	(6.16%, -)
	PL3	3	0.06	708	0.641	6.322	(16.39%, -)
	PL4	4 (coarsest)	0.09	210	0.641	6.419	(32.01%, -)
frictional ( $\mu = 0.4$ )	PF0	0 (finest)	0.005	1,222,330	0.640	6.045	(-, 1.53)
	PF1	1	0.01	152,795	0.640	6.032	(-, 1.58)
	PF2	2	0.03	5,662	0.640	6.007	(-, 1.59)
	PF3	3	0.06	708	0.641	6.051	(-, 1.86)
	PF4	4 (coarsest)	0.09	210	0.641	6.029	(-, 5.72)

**Section 4**, PG boxes made of varying particle sizes were used to construct an excavatable slope.

In addition to the macroscopic and microscopic fabric properties, it is also worthwhile to examine the mesoscale properties of a PG box. A critical mesoscale feature is the interconnected nature of the particles within a PG box. By overlapping, the contacting particles form an interconnected network [(Rothenburg & Bathurst, 1989; Yang, et al., 2017)]. The mesoscale fabric property associated with internal connectivity can be revealed by analyzing the statistics of the overlap vectors  $\delta^n = \delta^n n$ , which is the unit normal contact vector  $n$  scaled by the amount of overlap  $\delta^n$ . Here, the unit normal vector  $n$  depends on the particle chosen within a contacting particle pair  $i$  and  $j$  to compute the contact forces, e.g., particle  $i$  for  $n$  defined in Eq. (5). Using the symmetry of Newton's third law, the contact forces need to be computed only once, e.g., for particle  $i$ , instead of twice for the two contacting particles. In DEM simulations, particle ordinals can be used to select one particle in a pair, such as the one with the larger particle ordinal. The particles (shaded spheres) around the center of a PG box and their overlap vectors  $\{\delta_{ij} = \delta_{ij}^n n\}$  are visualized in Fig. 5(a) for illustration. The vector  $n$  is plotted at the center of mass of a particle  $i$  and points to the center of mass of particle  $j$ . As is shown in Fig. 5, for each overlap vector  $\delta_{ij}$  originating from particle  $i$ , there is always a corresponding overlap vector  $\delta_{ji}$  originating from particle  $j$ , where  $\delta_{ij} = -\delta_{ji}$ . Therefore, it is sufficient to consider the statistics of  $\delta_{ij}$  with respect to the polar angle  $\theta$  for  $[0, 90^\circ]$ , although the full range of  $\theta$  is  $[0, 180^\circ]$ .

The statistics of the normalized overlap vectors with respect to the polar angle are good indicators of the isotropy of the fabrics of a granular

packing. The mean values of the normalized overlap vectors at a polar angle  $\theta$  can be defined as

$$\bar{\delta}^n(\theta) = \frac{1}{N_{\theta_\delta}} \sum_{\theta_\delta \in [\theta - \frac{\Delta\theta}{2}, \theta + \frac{\Delta\theta}{2}]} \frac{|\delta_{ij}^n|}{r \sin(\theta)}, \quad (21)$$

where  $\theta_\delta$  and  $|\delta_{ij}^n|$  are the polar angle and the magnitude of an overlap vector  $\delta_{ij}^n$ ;  $N_{\theta_\delta}$  is the number of the overlap vectors whose polar angles  $\theta_\delta$  fall in the sampling range  $[\theta - \frac{\Delta\theta}{2}, \theta + \frac{\Delta\theta}{2}]$  with a sampling interval  $\Delta\theta$ . We computed  $\bar{\delta}^n$  for a set of sampling angles  $\{\theta_l^s\} = (l - 0.5)\Delta\theta$  with  $\Delta\theta = 5^\circ$  and  $l = 1, 2, 3, \dots, 18$  evenly and successively distributed between  $[0, 90^\circ]$ . The distribution of  $\bar{\delta}^n(\{\theta_l^s\})$  for PG boxes PL0 ~ PL4 created under frictionless condition are shown in Fig. 6 and for PG boxes PF0 ~ PF4 under frictional condition are shown in Fig. 7.

There are many sophisticated measurements to evaluate the fabrics in granular samples, ranging from the classical Satake-Oda fabric tensor [(Satake, 1982; Oda, 1982)] to a more recent stress-weighted fabric tensor [(Guo and Zhao, 2013)]. Advanced tensorial versions like Guo and Zhao (2013) are more descriptive, but require additional quantities such as inter-particle stresses, which may not be easily measured in experiments. On the other hand, the contact normal direction is a simple observable which can be derived from particle positions [(Krengel et al., 2023)] and can be measurable in experiment [(Ali et al., 2023)]. In this study, we utilized this simple observable to quantify the fabric property of PG boxes. As shown in Figs. 6–7, simple statistical quantities

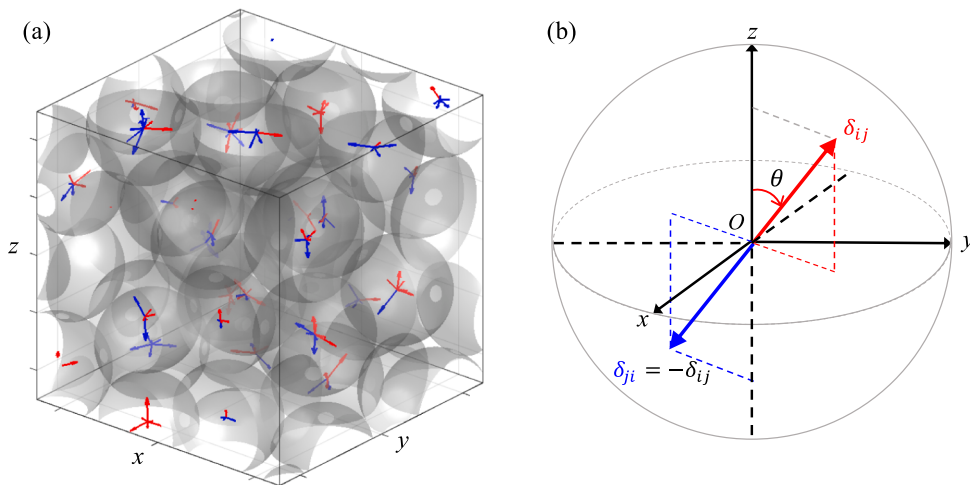


**Fig. 5.** (a) Enlarged view of the overlap vectors inside a unit PG box; here we plot an overlap vector  $\delta_{ij}$  from the center of mass of particle  $i$ ; due to the action-reaction principle, there is always a pair of  $\delta_{ij}$  (in red when  $i < j$ ) and  $\delta_{ji}$  (in blue when  $j < i$ ); (b) Polar angle  $\theta$  of  $\delta_{ij}$  against the z-axis: The average of  $\delta_{ij}$  within a range of polar angles  $[\theta - \Delta\theta/2, \theta + \Delta\theta/2]$  is measured to investigate the mesoscale fabric properties of a PG box.

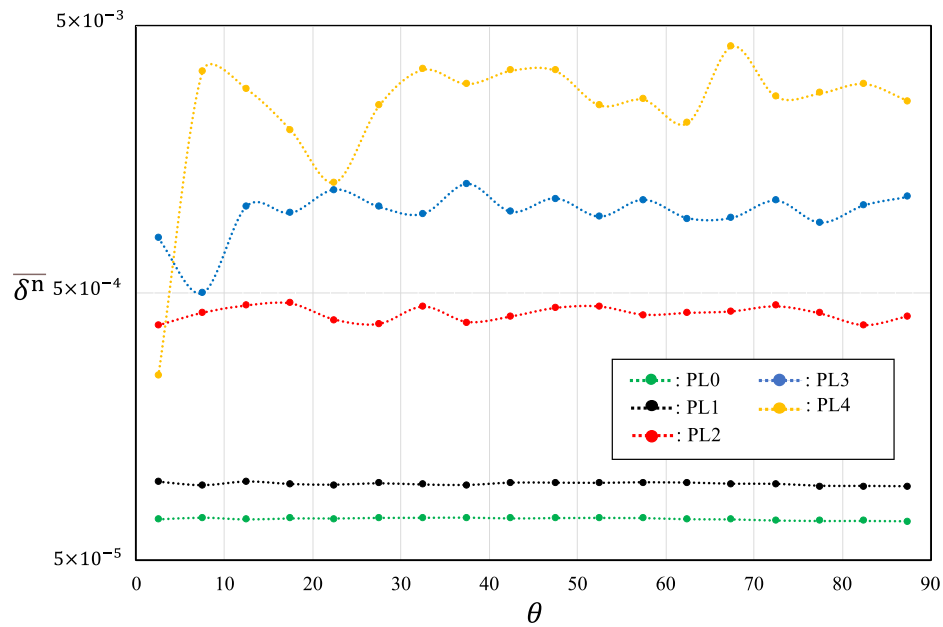


**Fig. 6.** Distribution of normalized overlap vectors over polar angles for frictionless PG boxes PL0 ~ PL4.

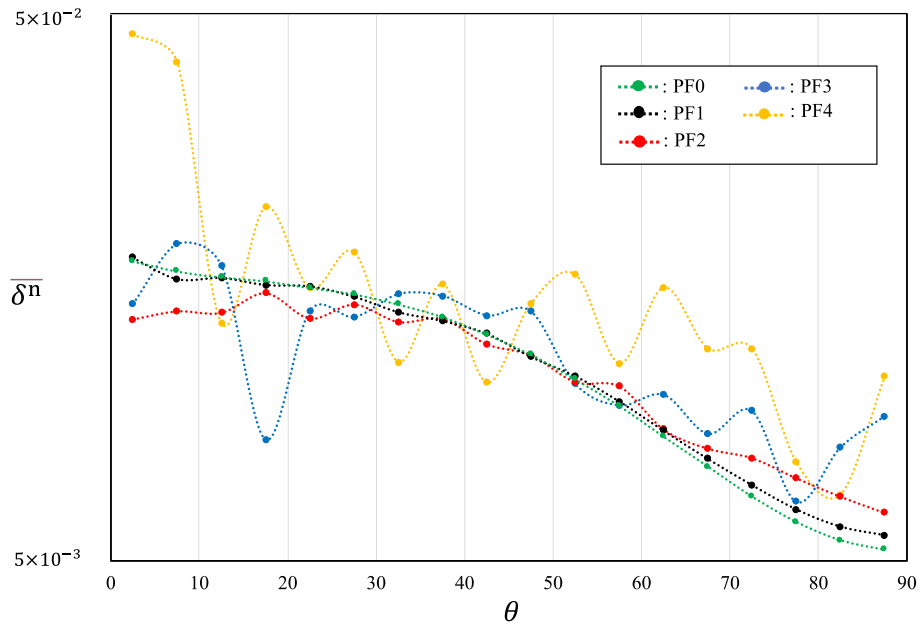


**Fig. 7.** Distribution of normalized overlap vectors over polar angles for PG boxes PF0 ~ PF4 created under friction.

describing the distributional properties of the normalized overlap vectors  $\bar{\delta}^n(\theta)$  may be sufficient to characterize the fabric properties of PG boxes. For distributions that converge to the uniform distribution, as shown in Fig. 6, the relative standard deviation (RSD), which describes the deviation from the mean value, is a simple measure of the deviation from isotropy. For distributions that resemble a bell shape with a long tail, as shown in Fig. 7, Kurtosis (Kurt), which measures the relative peakedness (or flatness) of a distribution compared to the normal distribution, can be used to quantify the anisotropy of PG boxes constructed under frictional conditions.

In the absence of friction, there will be no bias in the direction of gravitational sedimentation of particles. Therefore, ideally, the fabrics of PG boxes PL0 ~ PL4 are isotropic, and the distribution of overlap vectors should be uniform over the polar angle. The isotropy of fabric

can be confirmed from Fig. 6 for finer PG boxes, e.g., PL0 and PL1, whose distribution curve is flat and smooth. As the resolution becomes coarser, from PL2 to PL4, the distribution curve becomes more oscillatory. The oscillation was further quantified by the relative standard deviation (RSD) of each set of  $\{\bar{\delta}^n_l\}$  as

$$RSD = \frac{1}{\langle \bar{\delta}^n_l \rangle} \sqrt{\frac{1}{l_{max}} \sum_l (\bar{\delta}^n_l - \langle \bar{\delta}^n_l \rangle)^2}, \quad (22)$$

where  $\langle \cdot \rangle$  represents the average operation and  $l_{max} = 18$ . The RSD results for PG boxes PL0 ~ PL4 are summarized in Table 2. The RSD of PG boxes PL0 and PL1 converge to a small value of about 1%. In contrast, the coarsest PG box, PL4, has an RSD greater than 30%. It is thus clear that a finer PG box, composed of a larger number of particles,

has a smaller *RSD*, indicating a better fabric isotropy. We also confirmed that the *RSD* values for PG boxes were as low as about 1.0% for four more PG boxes with the same resolution as PL0 and PL1, respectively. From resolution level 1 to 0, the number of particles doubles, while the change in *RSD* is already sufficiently small (less than 0.5%). This is an indication that a PG box generated under frictionless conditions at resolution level 1 is sufficient to be considered as a homogeneous random granular packing with (statistically) isotropic fabric property.

In the case of frictional particle sedimentation, which is a more practical scenario from an engineering point of view, the gravity and friction would introduce an inherent anisotropy into a granular packing [(Chang & Yin, 2010)]. To study such anisotropy, we constructed PG boxes PF0 ~ PF4 with friction coefficient  $\mu = 0.4$ . The distributions of the normalized overlap vectors within these PG boxes over the polar angle are shown in Fig. 7. Unlike the flat distribution curves in Fig. 6 under frictionless conditions, the curves become (half) bell-shaped with peaks around  $\theta = 0^\circ$  and tails around  $\theta = 90^\circ$ . This means that the overlap vectors in the PG boxes PF0 ~ PF4 are preferentially aligned in the  $z$ -direction. The preference of the vertical direction ( $z$ -direction) over the horizontal direction is due to friction: Friction slows down the movement of the particles in the tangential directions, thus preventing the formation of contact in the horizontal direction compared to the vertical direction. For the finer PG boxes PF0 and PF1, the distribution curves are smooth and tend to converge. As the resolution becomes coarser, from PF2 to PF4, the distribution curve becomes more oscillatory. Although the corresponding *RSD* values for  $\delta_{ij}^n$  have been computed and are presented in Table 2 for completeness, this statistic is not informative because the oscillation is not around a flat line corresponding to the mean. To quantify the characteristics of these bell-shaped curves in Fig. 7, we computed their kurtosis, defined as

$$Kurt = \frac{\frac{1}{l_{\max}} \sum_l (\delta_l^n - \langle \delta_l^n \rangle)^4}{\left( \frac{1}{l_{\max}} \sum_l (\delta_l^n - \langle \delta_l^n \rangle)^2 \right)^2}. \quad (23)$$

Kurtosis is a measure of the sharpness or “tailedness” of a curve/distribution based on the fourth statistical moment. For a normal distribution, *Kurt* = 3. For “flat-topped” distributions, which have thinner tails and less sharp peaks than a normal distribution, *Kurt* < 3. This is the case for the distribution curves as shown in Fig. 7. As the resolution becomes finer (the particle size becomes smaller), the kurtosis converges to a value of about 1.5, as shown in Table 2. The smooth and converged distribution curves of PF0 and PF1, and the corresponding converged kurtosis values, indicate that anisotropy is an intrinsic property of the PG boxes created under frictional conditions. Therefore, our method can also construct PG boxes with converged mesoscale anisotropic fabrics.

Also note that the absolute values of the normalized overlap vector in Fig. 6 and Fig. 7 differ by orders of magnitude. This difference is caused by the different amount of compression of the initial sedimented samples to create PG boxes with equivalent volume fractions of 0.64. As explained in Sec. 2.3, the PG boxes are created by compressing sedimented samples, and the amount of compression depends on the difference between the volume fractions of the PG boxes and the initial samples. The initial volume fraction of the frictionless samples used to create PL# PG boxes was very close to the target value of 0.64, with a difference to the third decimal place, while the initial volume fraction of the frictional samples used to create PF# PG boxes was about 0.60. More compression was required to create PF# PG boxes, resulting in larger values for the averaged overlap vector magnitude in Fig. 7. The difference in the initial overlap at the modeling stage can be taken care of by setting it as  $\delta_{ij}^{n0}$  in Eq. (12) before applying external loads in subsequent DEM simulations.

### 3.2. Mechanical properties

A triaxial test is a common laboratory experiment used to measure the mechanical properties of soil and rock specimens. Similarly, numerical triaxial tests can be performed using DEM simulations to measure the mechanical properties of numerical specimens [(Thornton, 2000; Cui, et al., 2007; Gil & Alshibli, 2014; Kawamoto, et al., 2018)]. We performed numerical triaxial tests to investigate the mechanical properties of specimens made by PG boxes, focusing on the influence of the resolution of the PG boxes and the friction condition under which a PG box was prepared.

The setup for the numerical triaxial test is shown in Fig. 8(a). A cylindrical specimen of a diameter  $D = 0.2$  m and height  $H = 0.4$  m was subjected to a constant confining pressure and compressed by moving the top plate toward the bottom plate at a constant speed, corresponding to a load of constant axial strain rate. The forces on the plates were averaged over their area to measure the axial stress. A cylindrical specimen was prepared using the “glue-and-trim” modeling technique with PG boxes as described in Sec. 2.2 and illustrated in Fig. 3. A flexible membrane was used instead of a rigid wall in our numerical triaxial test, which can model the actual behavior of the rubber membrane and avoid suspicious boundary effects from a rigid wall [(Sakaguchi, et al., 2000; Gil & Alshibli, 2014; Qin, et al., 2021)]. The membrane was modeled by particles of the same size as the granules and deformed to achieve the target confining pressure. Snapshots of a typical numerical triaxial test using DEM are shown in Fig. 8(b). With the exception of the following three, the DEM parameters used to perform the numerical triaxial tests are the same as those listed in Table 1: i) the particle size  $r$  was set to 0.001 m; ii) the friction was set to a higher value  $\mu = 0.75$ ; iii) the parameters for bonding force were initialized to  $P_b = 13$  kPa,  $\mu_b = 10$ , and  $\chi_{\text{ini}} = 1.05$ . These parameters were chosen to reproduce a failure envelope comparable to laboratory tests on the undisturbed unsaturated volcanic ash soils typically found in the region of the Aso landslide [(Putra, et al., 2020)]. Since Putra et al. (2020) conducted direct-shear test instead of triaxial test, we focus on comparable failure envelope parameters  $\{c, \phi\}$  in Eq. (16) instead of stress-strain curves. The properties of the membrane particles were set to be the same as the specimen particles, except for a much softer stiffness: 1,000 times smaller than the Young’s modulus used for the specimen particles.

To make specimens from PG boxes with the same particle size  $r_s = 0.001$  m, the particles of size  $r_{\text{PG}}$  in a unit PG box must be rescaled to  $r_s$ , changing the box length from 1 m to  $r_s/r_{\text{PG}}$  m. As a result, the rescaled size of a finer unit PG box with smaller  $r_{\text{PG}}$  became larger than a coarse PG box with larger  $r_{\text{PG}}$ . Therefore, a smaller number of rescaled fine PG boxes are needed to fill a domain of the same size than rescaled coarse PG boxes. Different numbers of rescaled PG boxes were used for different resolutions to fill a rectangular area containing a specimen. Let  $nx$ ,  $ny$ ,  $nz$  be the number of PG boxes aligned along the  $x$ ,  $y$ , and  $z$  directions, respectively:  $1 \times 1 \times 2$  PG boxes PL0 (or PF0),  $2 \times 2 \times 4$  PG boxes PL1 (or PF1),  $6 \times 6 \times 12$  PG boxes PL2 (or PF2),  $12 \times 12 \times 24$  PG boxes PL3 (or PF3), and  $18 \times 18 \times 36$  PG boxes PL4 (or PF4) were connected to fill the domain to generate a specimen of corresponding resolution. The specimens composed of PG boxes PL# and PF# were labeled as SPL# and SPF#, respectively. For comparison, we also prepared a specimen labeled as SFF using the conventional free-fall technique. A total of 11 types of specimens were prepared for numerical triaxial testing.

As the initial conditions for a triaxial test, the tangential displacement was reset to  $\delta_{ij}^t = 0$  and the normal displacement forming the PG box was used to set  $\delta_{ij}^{n0}$  for a pair of initially contacting particles. This results in a stress-free initial state that eliminates any stress anisotropy while maintaining the fabric (connectivity) anisotropy that channels the distribution of new external loads. The state of the bond variable was initially activated, i.e.,  $B_{ij} = 1$ , for a pair of particles whose distance was within a threshold proportional to their particle size by a factor of  $\chi_{\text{ini}}^b$ ,

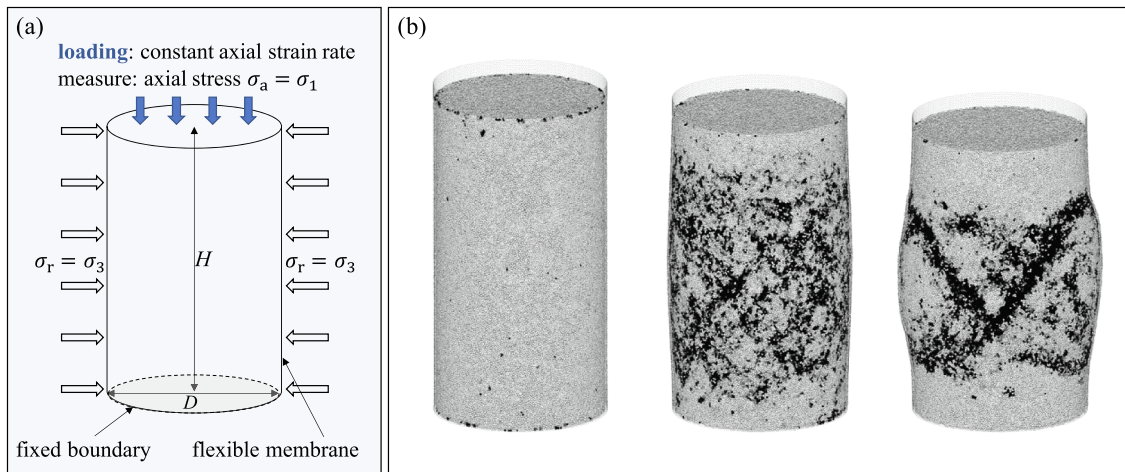


**Fig. 8.** (a) Setup: a specimen with diameter  $D = 200$  mm and height  $H = 400$  mm. (b) Snapshots during a numerical triaxial test: shear-band failure patterns were well reproduced, with the gray shading indicating particle rotation.

$$|\mathbf{x}_j - \mathbf{x}_i| < (r_i + r_j)\chi_{\text{ini}}^b. \quad (24)$$

Note that in Eq. (24), when  $\chi_{\text{ini}} = 1.0$ , only physically contacting particles are bonded, while when  $\chi_{\text{ini}} > 1.0$ , the influence range of bonding force becomes larger than the particle size. This increase in the influence range increases the number of bonded particle pairs within a numerical specimen and consequently increases its tensile strength [(Scholtès & Donzé, 2013)].

To quantify the macroscopic (specimen scale) property of a PG box, we measured the cohesion  $c$  and the internal friction angle  $\phi$  of the failure envelope of the corresponding specimen made of such a PG box. Numerical triaxial tests were performed with three confining pressures of 0, 100, and 200 kPa. The stress-strain results are summarized in Figs. 9 and 10, for specimens SPL# (from PG boxes PL# prepared without friction) and for specimens SPF# (from PG boxes PF# prepared with friction), respectively. The stress-strain results for SFF, the specimen prepared by the free-fall technique, are shown in Fig. 11, along with the SPL1 results for comparison. The failure envelope parameters

$(c, \phi)$  were calculated from the corresponding Mohr's circles of different confining pressures and are summarized in Table 4. Note that packing density is an important factor affecting the mechanical properties. To check the influence from specimen resolution, the specimens were dense made of PG boxes with a fixed volume fraction of about 0.64 to exclude the influence of packing density.

The stress-strain curves of the specimens SPL# made from PG boxes PL# prepared under frictionless conditions are shown in Fig. 9. Without external confining pressure, all specimens exhibited a similar stress-strain curve with finite failure strength. This strength allows the DEM particles to form a stable slope with excavatable surficial soils. When the confining pressure is increased to 100 kPa, the stress-strain behavior is consistent for specimens of different resolution levels, except for a (softening) deviation observed for specimen SPL4 of the coarsest resolution. When the confining pressure reaches 200 kPa, the resolution level has a noticeable effect on the peak stress and strain. It is worth noting that the post-failure stress tends to converge when the strain becomes large enough. This indicates that the differences in mesoscale

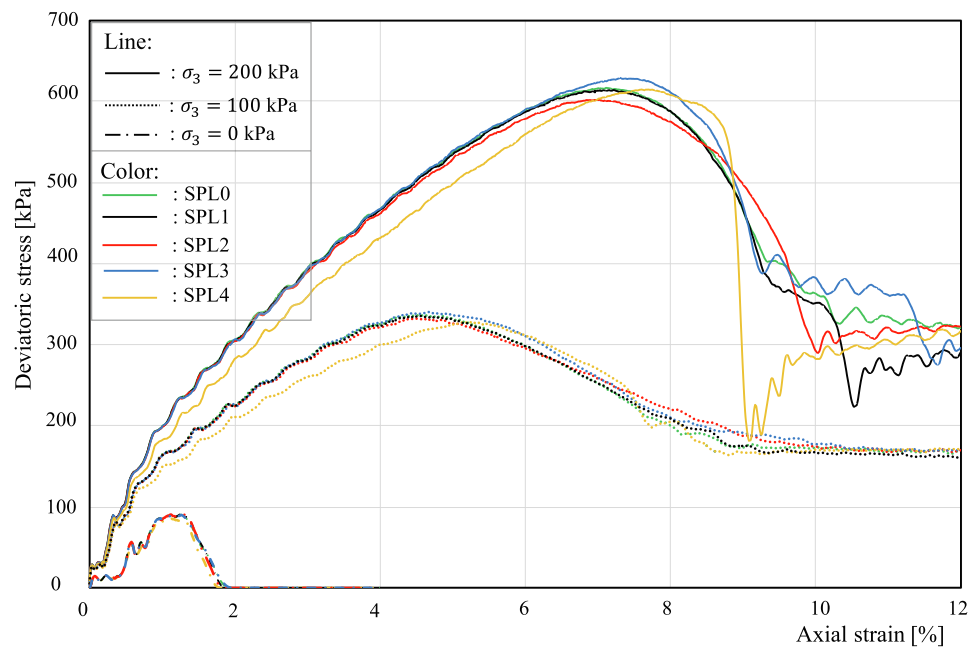


**Fig. 9.** Stress-strain curves from numerical triaxial tests on specimens SPL0 ~ SPL4, made by PG boxes PL0 ~ PL4.

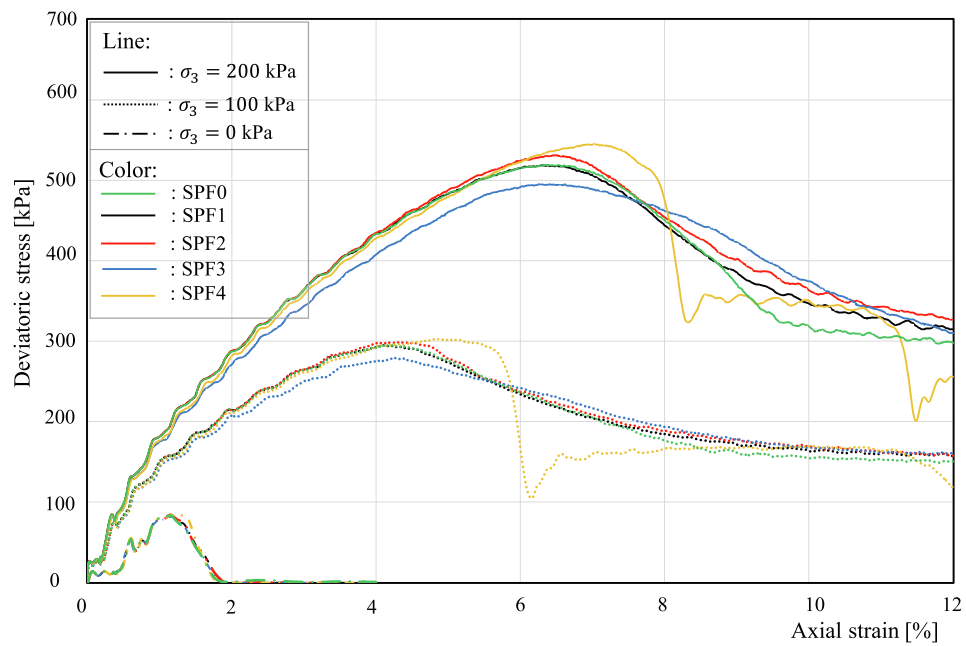


**Fig. 10.** Stress–strain curves from numerical triaxial tests on specimens SPF0 ~ SPF4, made by PG boxes PFO ~ PF4.

fabrics introduced by the PG box resolution are “smoothed out” by large deformations. There is also very good agreement between the stress–strain curves of SPL0 and SPL1 up to (and slightly beyond) the failure strain. The convergence means that PG boxes PL1 are fine enough to generate initially isotropic DEM models for the simulations focused on failure initiation, e.g., initiation of a landslide.

The stress–strain curves of the specimens SPF# made from PG boxes PF# prepared with friction are shown in Fig. 10. The general trends and characteristics of the curves are similar to those of the isotropic specimens in Fig. 9: a finite strength without confining pressure, consistent peak stresses with small deviations at moderate and high confining pressures, and an increase in deviation with increasing coarseness of resolution. For specimens made from PG boxes with finer resolutions, the stress–strain curves of SPF0 and SPF1 tend to converge up to (and

slightly beyond) the failure strain, indicating that PG boxes PF1 are fine enough to generate initially anisotropic DEM models. For specimen SPF4, made from the coarsest PG boxes PF4, an abrupt drop from the peak stress to the post-failure stress is already observed at 100 kPa confining pressure, which does not appear until 200 kPa for SPL4. Comparing Figs. 9 and 10, another noticeable difference between SPF# and SPL# is the decrease in peak stress at failure. This decrease indicates that the macroscopic material strength of a PG box is influenced by its mesoscopic fabrics: anisotropic specimens SPF# have lower shear strength compared to isotropic specimens SPL#.

We also directly prepared specimens SFF using the free-fall technique and performed corresponding numerical triaxial tests. The stress–strain curves for SFF are shown in Fig. 11. Since the SFF specimens were prepared under frictionless conditions to obtain a comparable volume

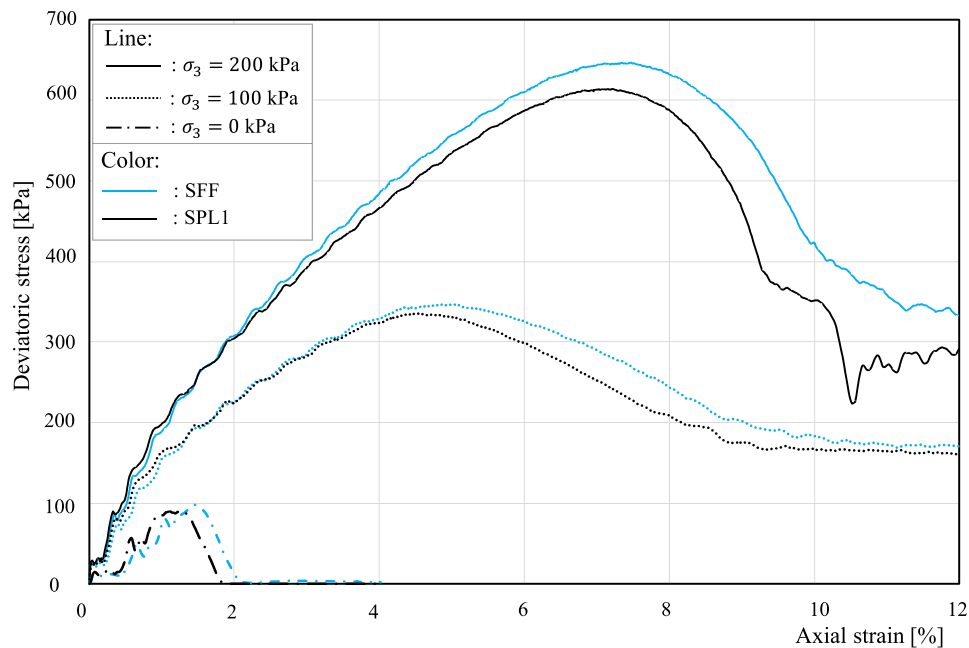


**Fig. 11.** Stress–strain curves from numerical triaxial tests on specimens made from free-falling particles. SPL1 results are shown for comparison.

**Table 3**

Summary of the residual and peak deviatoric stresses from the numerical triaxial experiments in Figs. 9–11 for the isotropic SPL# specimen, the anisotropic SPF# specimen, and the conventional free-fall SFF specimen. The residual stress is measured as the average of the axial strain range between 11% and 12%.

Specimen (frictionless)	SFF	SPL0	SPL1	SPL2	SPL3	SPL4	Confining stress
Residual stress [kPa]	5.92	9.7	7.93	5.99	6.95	8.89	$\sigma_3 = 0$ kPa
Peak stress [kPa]	98.36	90.62	91.45	91.36	90.12	85.85	
Residual to peak ratio [%]	6.02	10.7	8.67	6.56	7.71	10.35	
Residual stress [kPa]	171.19	168.12	162.89	169.03	169.91	170.39	$\sigma_3 = 100$ kPa
Peak stress [kPa]	346.75	336.6	335.48	332.19	340.44	328.1	
Residual to peak ratio [%]	49.37	49.95	48.55	50.88	49.91	51.93	
Residual stress [kPa]	343.25	326.06	281.81	319.55	318.44	310.11	$\sigma_3 = 200$ kPa
Peak stress [kPa]	647.13	616.72	614.17	602.16	629.08	614.98	
Residual to peak ratio [%]	53.04	52.87	45.89	53.07	50.62	50.43	
Specimen (frictional)	SPF0	SPF1	SPF2	SPF3	SPF4		Confining stress
Residual stress [kPa]		3.76	3.34	4.18	8.23	8.5	$\sigma_3 = 0$ kPa
Peak stress [kPa]		84.01	84.89	84.75	82.17	84.39	
Residual to peak ratio [%]		4.47	3.94	4.93	10.02	10.07	
Residual stress [kPa]		151.59	159.66	160.58	161.33	149.16	$\sigma_3 = 100$ kPa
Peak stress [kPa]		295.53	295.29	298.97	279.49	303.24	
Residual to peak ratio [%]		51.29	54.07	53.71	57.72	49.19	
Residual stress [kPa]		302.2	320.13	334.47	323.87	262.64	$\sigma_3 = 200$ kPa
Peak stress [kPa]		519.11	518.73	531	495.17	544.86	
Residual to peak ratio [%]		58.21	61.71	62.99	65.41	48.2	

**Table 4**

Failure envelope parameters, the cohesion  $c$  and the internal friction angle  $\phi$  as in Eq. (16), for the isotropic specimens SPL# and the anisotropic specimens SPF#. The relative errors (rel. error) were calculated with respect to  $c = 22.80$  kPa and  $\phi = 35.60^\circ$  for the specimens SFF made directly from the free-fall technique.

Specimen label	SPL0	SPL1	SPL2	SPL3	SPL4
$c$ [kPa]	22.34	22.49	22.90	21.73	20.46
rel. err. [%]	2.02	1.36	0.44	4.69	10.26
$\phi$ [°]	34.64	34.58	34.18	35.11	34.81
rel. err. [%]	2.70	2.87	3.99	1.38	2.22
Specimen label	SPF0	SPF1	SPF2	SPF3	SPF4
$c$ [kPa]	23.00	23.23	22.74	22.58	22.16
rel. err. [%]	0.88	1.89	0.26	0.96	2.81
$\phi$ [°]	31.43	31.39	31.87	30.58	32.41
rel. err. [%]	11.71	11.83	10.48	14.10	8.96

fraction, the SPL1 results representing the isotropic specimens are included for comparison. As shown in Fig. 11, the shear strength of SFF specimens is a few percent higher than that of SPL1. This may be due to a limitation of the PG box-based modeling technique: when more than one PG box is connected to fill a domain for modeling, a periodic pattern characterized by the PG box size is introduced into the model. This artificial periodicity may contribute to the weakening of the strength of models made from connected PG boxes compared to models made from direct gravitational settling. Another factor that may contribute to the observed difference in the model strength is the wall effect in the preparation of SFF: the fabrics near the cylindrical wall were found to be different from the isotropic inner region. A causal explanation for this difference in strength is still beyond our reach and will remain as a future work. For anisotropic specimens, no comparison is made between two modeling techniques because it is difficult to prepare specimens using free-fall to reach a volume fraction of 0.64 as in SPF#. Nevertheless, a similar decrease in strength can be expected due to the artificial periodicity. From an engineering point of view, there are large variations both in soils and rocks and in laboratory measurements, see e.g. [Duncan & Wright, 2005]. Our observed strength difference (of a few percent) would not be critical for landslide simulations.

The residual shear strength is important for slope stability analysis, such as determining the residual slope angle and the runout distance. Therefore, we have summarized in Table 3 the residual stress, the peak stress and the ratio between them from the numerical triaxial tests. The residual stress was measured as the average stress corresponding to the axial strain range of 11% to 12% in Figs. 9–11. As can be seen from the table, both the residual stress and the peak stress are small in the case of

zero confining pressure, and the residual stress varies from 6 to 10% of the corresponding peak stress for the specimens made under frictionless condition (SPL# and SFF). For the specimens made under frictional condition (SPF#), the residual stress varies from 4 to 10% of the corresponding peak stress and increases with the increase in particle size (coarseness). The particle-size dependence for samples of equivalent packing density observed here is consistent with experimental studies on residual shear strength of soils [(Tiwari and Marui, 2000)]. As the confining pressure increases, the residual stress, peak stress and their ratio increase. For SPL# and SFF specimens, the ratio of residual stress to peak stress ratio is about 50%, and there is no significant difference in this ratio between the confining pressures of 100 kPa and 200 kPa. For SPF# specimens, except for the coarsest SPF5, the ratio of residual stress to peak stress increases from about 50% to about 60% as the confining pressure increases from 100 kPa to 200 kPa.

The failure envelope parameters in Eq. (16) are summarized in Table 4 for the isotropic specimens SPL# and the anisotropic specimens SPF# made from the PG boxes prepared under frictionless and frictional conditions, respectively. The envelope parameters for the specimens SFF made under frictionless conditions are used as reference values to calculate the relative errors. For the isotropic specimens SPL#, the relative errors in the cohesion parameter  $c$  are less than 5%, except for the coarsest specimen SPL4; the relative errors in the internal friction angle  $\phi$  are less than 4% for the specimens of all resolution levels. For the anisotropic specimens SPF#, the relative errors in  $c$  are generally smaller than that for SPL#. Even for the coarsest specimen SPF4, it is less than 3%. In contrast, the relative errors in  $\phi$  are much larger, generally around 10%. Note also that the variations in the relative errors between

the same type of specimen at different resolution levels are relatively small, except for the coarsest. From these comparisons, it can be concluded that the internal friction of a PG box is much more affected by its inherent fabrics, whether they are isotropic or anisotropic, than by the resolution levels. The cohesion parameter, on the other hand, is less sensitive to the fabric properties, unless the resolution is too coarse.

To confirm the accuracy of the envelope parameters calculated above (and the soundness of the conclusion based on them), for the finer resolution levels 0 and 1, we made five different SPL0 and SPL1 from five different PG boxes PL0 and PL1 (by introducing initial random velocities to the particles to be settled), performed numerical triaxial tests, and calculated the envelope parameters. The relative error between the five SPL0 is about 0.88% for  $c$ , and about 0.07% for  $\phi$ . The relative error between the five SPL1 is about 1.0% for  $c$ , and about 0.11% for  $\phi$ . Such a small relative error indicates a good reproducibility of the numerical simulations, which is generally difficult to achieve in laboratory experiments on soils. One difficulty in laboratory testing, which is attributed to the large variation in measured laboratory mechanical properties, is the preparation of soil specimens with well-controlled mesoscopic properties: as can be seen from our simulations, even at the same volume fraction, a change in the mesoscopic fabrics alters the macroscopic mechanical properties.

#### 4. Large-scale DEM model for Aso-bridge landslide

The Aso Bridge landslide is a typical large-scale destructive landslide with lasting socioeconomic impacts, highlighting the importance of disaster preparedness for infrastructure and transportation networks. It occurred on April 16, 2016, in Kumamoto Prefecture, Japan, triggered by a magnitude  $M_w = 7.0$  ( $M_{jma} = 7.3$ ) earthquake that struck the region [(Dang, et al., 2016)]. Field observations showed that the sliding area has a tongue-like shape, e.g., see Fig. 1(a) as a front view. The area is estimated to have an average width of about 195 m and a length of about 705 m [(Song, et al., 2019)]. The estimated area ranges from about 130,000 m<sup>2</sup> [(Song, et al., 2019)] to 180,000 m<sup>2</sup> [(Hung, et al., 2019)], and the estimated total volume is nearly 2 million m<sup>3</sup> [(Song, et al., 2019)]. The massive debris flow rushed onto the railroad and highway, destroyed the bridge over the Kurokawa River, and was deposited there [(Dang, et al., 2016)]. Although no deaths were reported as a direct result of the landslide, it took 4–5 years after the landslide to rebuild the disrupted transportation networks.

High-resolution numerical simulations are needed to better assess the impact forces on key infrastructure from large-scale landslides, such as the Aso Bridge landslides. Conventional simulations using coarse resolution models can reproduce the runout characteristics [(Dai, et al., 2016; Hung, et al., 2019; Lai, et al., 2022)]. However, the error introduced by the coarse resolution is too large to be ignored when assessing the impact forces on structures and designing mitigation measures. Taking the simulations of the Aso Bridge landslide as an example, there are DEM and SPH simulations in the literature, e.g., Hung et al. (2019) used 2D DEM particles with a diameter of 1 to 2 m; Dai et al. (2016) used 3D SPH particles with a diameter of 7 m. As a simple analysis, assume that a spherical particle modeling water with diameters of 1.5 m and 7 m has a weight of about 1.8 t and 180 t, respectively, which is equivalent to the average weight of a car and the weight of a commercial airplane (e.g., Boeing 747–400). To evaluate the impact of sliding masses on an engineering structure, the difference introduced by one particle in a coarse-resolution simulation is equivalent to the difference introduced by a car or even by an airplane. The need to improve the resolution of numerical models is clear from this simple analysis.

We used the PG box-based method to construct high-resolution DEM models for the Aso Bridge landslide. Similar procedures as shown in Fig. 3 for the construction of cylindrical specimens were used to construct the slope model. The main difference is that the boundary

surfaces for trimming are more complicated. The following describes the construction of high-resolution DEM slope models:

- 1) First, the surfaces of the slope before and after the landslide were constructed. For the pre-landslide surface, satellite image-based AW3D<sup>1</sup> topology data with 50 cm resolution of the region were used to construct the slope surface, see Fig. 1(b). For the surface after the landslide, a coarser 5 m resolution post-landslide digital elevation model data was used. This post-landslide surface was then used to determine a main rupture surface as indicated by the blue area in Fig. 1(b).
- 2) Unit PG boxes were then connected to fill a domain of 800 m × 500 m × 600 m. Because the slope model is much larger than a unit PG box, instead of scaling down the particle size of a PG box to fill the domain as in the construction of cylindrical specimens, we must scale up the particle size to a defined value. For example, using a unit PG box with particles of size  $r_{PG} = 0.001$  m to model a slope with particle size  $r_s = 0.05$  m, the unit box length is scaled up from 1 m to  $r_s/r_{PG} = 50$  m, and consequently 16 × 10 × 12 scaled-up unit boxes are needed to fill the 800 m × 500 m × 600 m domain.
- 3) Next, the domain composed of PG boxes was trimmed vertically by two boundary surfaces. The pre-slide slope surface was used as the upper boundary surface. The lower boundary surface was constructed from the minimum between the pre-slide and post-slide surfaces and was shifted downward by 6 m. This resulted in a finite-thickness slope model composed of the same type of DEM particles, as opposed to conventional modeling of the slope surface as a fixed boundary. Particles above the main rupture surface identified in step 1) were labeled as initially released earth masses.
- 4) Finally, a sedimentation process was simulated to obtain a stable slope model for subsequent landslide simulations. In this sedimentation simulation, the gravity and binding forces were turned on and the particle density was set to 2.4 g/cm<sup>3</sup>, to model the black volcanic ash in the landslide region [(Putra, et al., 2020)]. There may be some sporadically debonded particle pairs where the bond becomes weaker than the stress induced by the imposition of gravity during this sedimentation stage, while the slope as a whole is stable with no noticeable slip before triggering. After sedimentation, the particles in the model reached their new equilibrium positions to account for the adjusted particle density. The deformation in this sedimentation is too small to cause a noticeable change in the slope surface for the Young's modulus considered (100 MPa).

A demonstration of a slope model constructed using the PG box method for the Aso Bridge landslide is shown in Fig. 12 using 6.5 billion particles. The maximum particle radius in this model was only 5 cm, the finest large-scale DEM slope model to the best of our knowledge. Except for the fixed bottom and side walls, all particles in the model are mobile depending on the balance between gravity and binding forces, resulting in an excavatable slope during the sliding process. The 5-centimeter resolution here is a limit imposed by the capability and availability of the computing resources, not by the modeling method or the actual situation (where typical soils are below the sub-micrometer scale). One scenario for using such a high-resolution landslide model is to assess the safety of critical infrastructure: for example, to assess the impact force of a potential landslide on a bridge, a particle size of 1 m may be too coarse according to the above analysis (that a spherical water particle with a diameter of 1.5 m has a weight of about 1.8 t), while a particle size of 5 cm may be tolerable (if the sliding mass contains mainly soil). Whether a resolution is effective depends on the intended use of the landslide simulations. Our method provides a robust way to construct slope models of different resolutions for landslide simulations.

<sup>1</sup> AW3D Enhanced & AW3D Ortho (C) 2022 Maxar Technologies. NTT DATA Corporation.

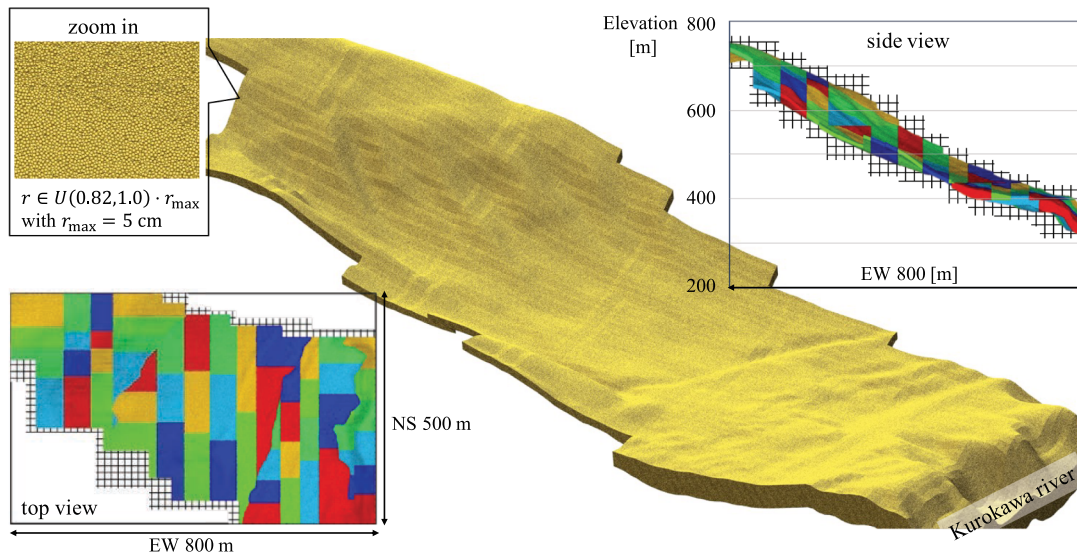


**Fig. 12.** Visualization of a finite-thickness slope model constructed using the PG box-based method: It is composed of 6.5 billion particles with a maximum radius  $r_{\max}$  of 5 cm. The slope model is located inside a box of size 800 m  $\times$  500 m  $\times$  600 m. The top and side views of the model are shown. The colored areas illustrate the initial three-dimensional domain decomposition for parallelization among different CPUs.

To verify the ability to simulate soil excavation, we performed a test landslide simulation using a coarse slope model composed of approximately 8 million particles with a maximum radius of 0.5 m. In the test simulation, we did not consider the triggering of the landslide by the seismic wave, which remains as a future work. For simplicity, as in many post-failure simulations [(Hung, et al., 2019; Wang & Sassa, 2010; Dai, et al., 2016)], the particles located above the identified main rupture surface, see the blue area in Fig. 1(b), were released as the start of the landslide. The release was realized by breaking the bonds for particle pairs along the identified main rupture surface. Snapshots of different stages of the simulated landslide are shown in Fig. 13, with the initial surface particles visualized in green and the underlying particles in brown. As can be seen in Fig. 13 (b-d), the expansion of the sliding region was accompanied by the removal and entrainment of surface material in the downstream direction. Remnants of the surface materials from the initial sliding region can also be observed scattered along the

sliding path, see e.g., Fig. 13 (d), which is consistent with visual evidence from early field observations of remnants of the surface vegetation. This excavation and deposition of surficial materials is rarely captured and reported in numerical simulations of large-scale landslides in the literature, (partly) due to resolution limitations. A more detailed analysis of the simulation results remains as a follow-up study.

As a further demonstration, we compared the simulation results of different grain sizes with the actual situation of the landslide in Fig. 14. According to a survey conducted by the Japan Society of Erosion Control Engineering (JSECE), in addition to the main landslide zone as shown in Fig. 1 (b), there was a secondary landslide zone in the downstream area, starting from the location just pass the JR railroad and the National Route 57 [(JSECE, 2016)]. Accordingly, in this demonstration, we also triggered the secondary landslide simultaneously with the main landslide, see the insets in Fig. 14 for the initial location of the secondary sliding zone. Since the particle properties are the same except for the

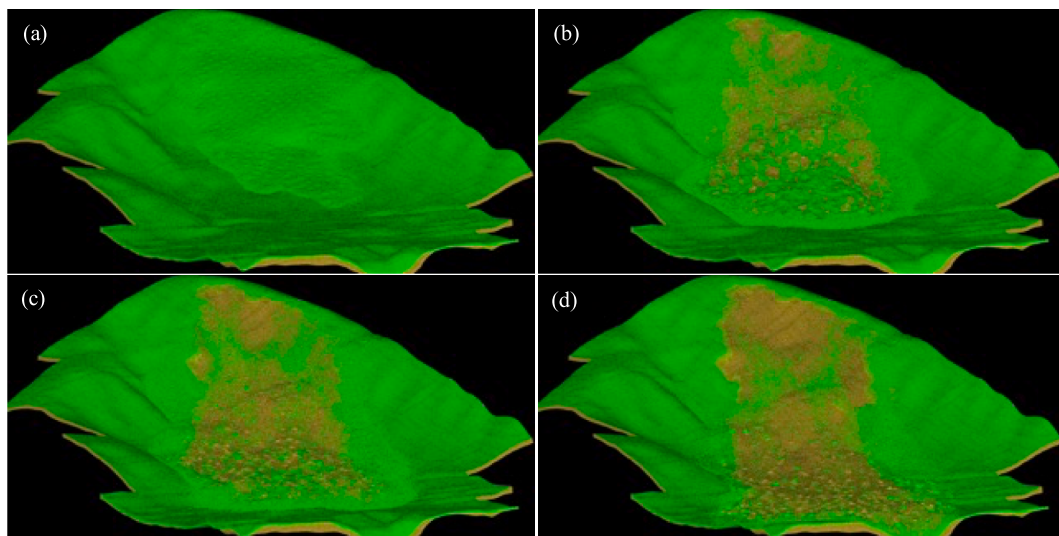


**Fig. 13.** Snapshots from a test simulation of the Aso Bridge landslide: (a) Immediately after the triggering of the landslide by breaking the bonds between the particle pairs along the main rupture surface; (b) Growth of the sliding region, where the removal and entrainment of surface materials are clearly visible; (c) The toe reached the railroad and highway, see Fig. 1 (a) and (b); (d) The toe reached the bank of the Kurokawa River and flowed into the river.

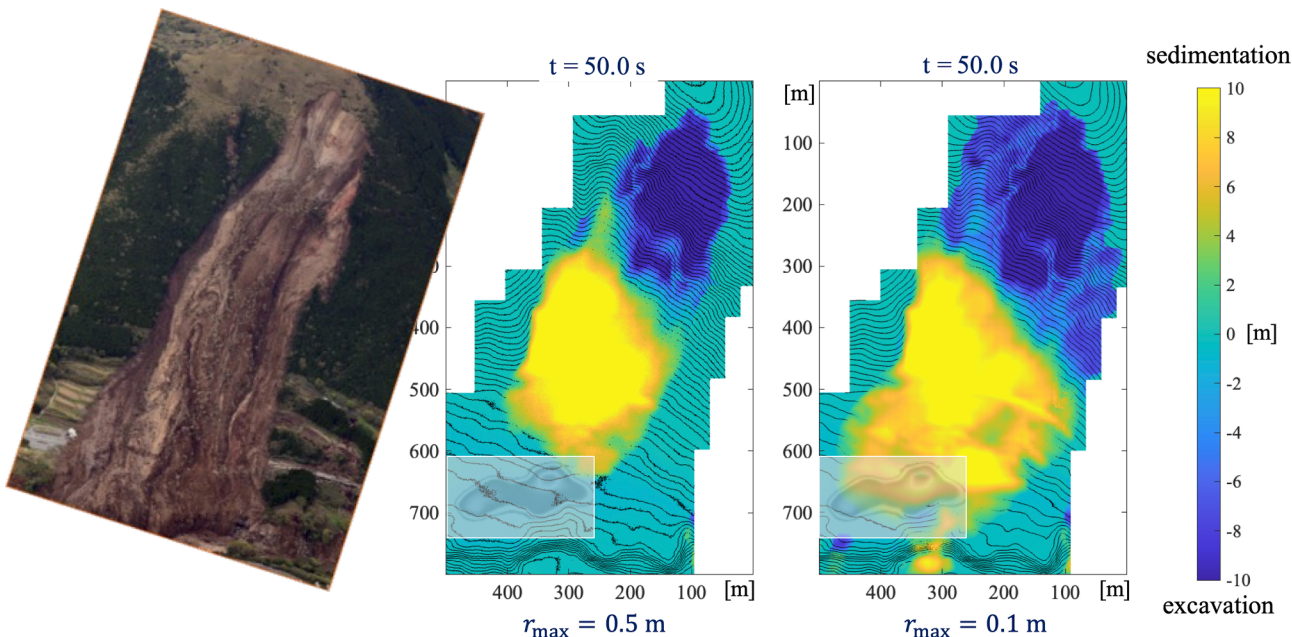


**Fig. 14.** Particle size effect: Aerial photo (left), simulations with maximum particle radii of 0.5 m (center) and 0.1 m (right) for the Aso Bridge landslide. The landslides were triggered at  $t = 5.0$  s.

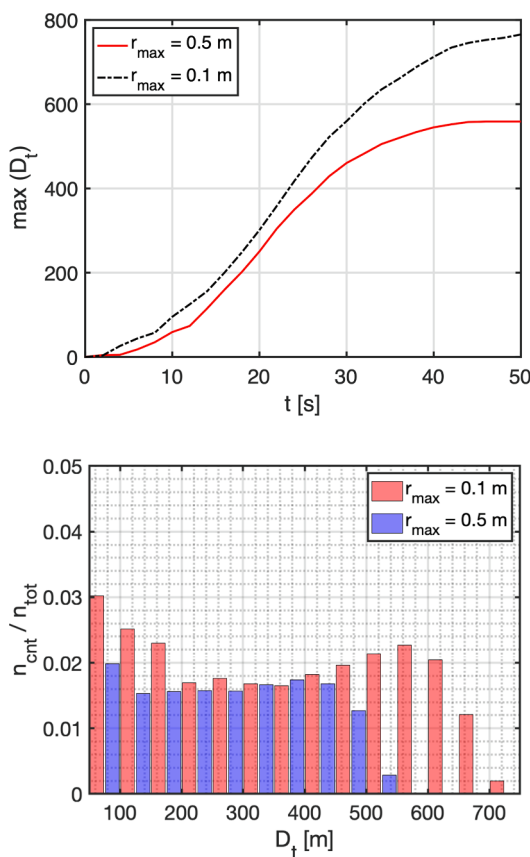


**Fig. 15.** Top: The maximal of the travel distance  $D_t$  at each output time step  $T_i$  (with interval  $\Delta T = 2$  s); Bottom: the histogram of the particle counts  $n_{\text{cnt}}$  normalized by the total number of particles in the simulation  $n_{\text{tot}}$  (about 832 and 8 million in the finer and coarser setting, respectively) according to the travel distance of particles at the end of simulation ( $t = T_{25} = 50$  s). The statistics for  $D_t > 50$  m is shown with a 50 m bin width in the histogram, while the majority of particles (bins not omitted) travel less than 50 m.

particle size, the grain size effect can be seen immediately from Fig. 14: For the coarse grains ( $r_{\max} = 0.5$  m), the debris from the main landslide zone is mainly deposited in front of the secondary landslide zone, where the slope is gentle and the depositional area is sufficiently wide, as can be seen from the terrain model in Fig. 1 (b) and the high-resolution DEM model in Fig. 12. This is a clear demonstration of how local topography/landscape affects the movement and deposition of earth masses. When the finer grains ( $r_{\max} = 0.1$  m) are released from the main landslide zone, they can move over the secondary landslide zone and push the released masses in the secondary landslide zone further down towards the river. This indicates that the grain size also significantly influences the movement and deposition of earth masses. Compared to the aerial photo, the fine-grain simulation is more consistent with the actual situation in terms of the area affected by the landslide.

In Fig. 15, we summarize a quantitative analysis from a relatively coarse time-resolution output of particle positions in the two trial simulations with fine and coarse grain sizes, i.e., with  $r_{\max} = 0.1$  m, and  $r_{\max} = 0.5$  m, respectively. In a DEM simulation, from the position data, we can trace the trajectory a particle and compute its travel distance  $D_t(T_i)$  by adding the magnitude of the displacement between two output instances  $T_{i-1}$  and  $T_i$ ,

$$D_t(T_i) = \sum_{i=1}^{\text{nstep}} |\mathbf{x}(T_i) - \mathbf{x}(T_{i-1})|, \quad (25)$$

where  $\mathbf{x}(t)$  is the position vector of the center of mass of particle at time  $t$ . In the trial simulations, we output the position data in interval  $\Delta t = T_i - T_{i-1} = 2$  s (and  $\text{nstep} = 25$  for a 50 s simulation). A coarse time-resolution output was chosen because handling the time-series of output data from a large-scale simulation is nontrivial: the fine grain simulation here contained a total number of particles  $n_{\text{tot}}$  over 832 million and the size of the position data of 26 time instances (including  $t = 0$  s) could be roughly estimated to surpass 500 GB (832 M particles  $\times$  3 components  $\times$  26 steps  $\times$  8 Bytes) if one only output the 3 position coordinates for a particle. The maximal travel distance of particles  $\max(D_t)$  is presented in Fig. 15, top. It is clearly seen that the maximal travel distance for the fine particles ( $r_{\max} = 0.1$  m) always exceeds the coarse particles ( $r_{\max} = 0.5$  m). This higher mobility of fine grains is not limited to a few particles. As can be seen from the normalized histogram in Fig. 15, bottom, there is only a small fraction of particles in the coarse-

grain simulation travelled over 500 m, while the fraction of particles is much larger in the fine-grain simulation that traveled over the same 500 m distance. Since the other conditions were controlled to be consistent, the results here show clearly the influence of particle size on landslide run-out distance: small particles in a fine-grain simulation have higher mobility than large particles in a coarse-grain simulation. It remains interesting for future work to see whether and how runout would saturate with particle size.

How particle size and distribution affect granular flows (and landslides) is an open question with contradicting results in literature: e.g., Lai et al. (2017) pointed out that particle size distribution (and the small constituents) may play an important role in high flowability ([Lai et al. 2017]). Cabrera and Estrada (2021) argued that the particle resolution in Lai's settings was insufficient, i.e., the system-to-particle size ratio was too small. Once the column width is sufficiently large compared to particle size, the size distribution would become insignificant ([Cabrera and Estrada 2021]). It should be noted that both studies were focused on a specific setting: the collapse of columns of granular materials which forms granular flows and eventually granular heaps. This setting is not directly comparable to actual landslides in which the granular materials slide longer distances to allow size segregation to sufficiently develop. Nevertheless, our result which shows the model with smaller particles leads to longer runout distance is consistent with Cabrera and Estrada's result of an increasing column flowability with a decrease in mean particle size. It is an interesting future work to check whether similar saturation of mobility also occurs for slopes as observed in the heap formation settings.

Note that these simulations are not intended and should not be interpreted as a replication of the Aso Bridge landslide, where nearly 90% of the released earth mass was transported to the river ([JSECE, 2016]). There are several reasons for this discrepancy with the actual situation: The simulation assumed the same type of material for the entire slope, whereas the actual slope consists of regions of different materials with different strengths. The friction in the simulation was rather high ( $\mu = 0.75$ ), while during the landslide some lubrication effects may effectively reduce the friction. Nevertheless, two things are clear from our demonstration: the local landscape has a large influence on the excavation and deposition of sliding masses; and, assuming that the material properties are well-tuned, the grain size influences not only the runout distance but also the spread of the landslide. This indicates the need for finer models for landslide simulations. It is possible to tune the material properties to obtain consistent influence area and runout distance with coarse grains (e.g., with a surface friction as low as 0.08 ([Hung et al., 2019])). However, to make the models more predictive, finer resolutions are preferable.

This sub-meter scale test simulation is still one of the finest 3D simulations of large-scale landslides compared to the published literature, although the slope model used is described as "coarse" compared to the finest model in Fig. 12. The verisimilitude/realism demonstrated by the test simulation highlights the potential for simulation results to be obtained from even finer slope models. In addition, the grain size-dependent runout and spread of the landslide observed in the simulations under the same conditions (except for particle size) suggest further study.

## 5. Discussion: Advantages and limitations of the PG box-based method

The advantages of the PG box-based method for constructing large-scale models are its efficiency and flexibility. The efficiency becomes significant when constructing models with millions or even billions of particles, such as the one shown in Fig. 12. In comparison, using the free-fall method to directly generate such a large slope model requires first implementing an inclined gravity field against the local surface topography with parallelization, which requires considerable coding effort and skill. The direct free-fall method then requires a sedimentation process that is computationally expensive for billions of particles. Even

for simple model geometries such as a rectangular box ([Furuichi, et al., 2017; Furuichi, et al., 2018]), the cost of the free-fall method for constructing models with billions of particles was non-trivial: it took about 12 h of the entire K computer, the world's No.1 supercomputer, around 2011 and 2012. To construct a model based on the actual slope topology, as shown in Fig. 12, it took about 5 h using 5,120 CPUs (245,760 cores) of Fugaku,<sup>2</sup> currently one of the world's fastest supercomputers. In contrast, using prepared PG boxes with about 200 thousand particles (the same resolution as PL1/PF1), it took only a few minutes to construct the slope model with 6.5 billion particles using the same number of CPUs on Fugaku. The cost of preparing a PG box with 200 thousand particles is negligible in terms of CPU hours: about 30 h with a single 48-core CPU, compared to hours with thousands of CPUs consumed by the direct free-fall method. As exemplified by the 5 cm resolution slope model for the Aso Bridge landslide, the proposed PG box-based method can drastically reduce the (implementation and computational) cost of constructing fine-resolution DEM models with complicated geometry. Nevertheless, we should admit that the advantage of the modeling technique is limited to the model construction stage, large-scale DEM simulations of the landslide process remain time-consuming, for which parallelization efficiency requires further improvement.

Another advantage of the PG-based method is its flexibility: PG boxes with different resolutions and calibrated properties can be prepared in advance. In contrast, the properties of a model and how they vary within a model, especially a large scale model built using the direct free-fall method, are not known until after the model has been constructed. From the quality analysis of the PG boxes in Sec. 3, it is clear that the mesoscale fabric properties converge with increasing resolution. Also, the influence of the resolution on the macroscopic failure envelope parameters has relatively small variations compared to typical experimental results on soils, except for very coarse resolutions. When preparing PG boxes for one's own needs, a resolution sufficient for the target problem can be determined in advance by performing numerical tests (triaxial or other types) on specimens constructed from the PG boxes, as we presented in Sec. 3. In addition to the ease of controlling model properties, the flexibility of the PG box-based method also comes from the separation of the PG box construction from the DEM model construction. Obviously, it is much easier to develop code and run simulations on a desktop machine than on a supercomputer. As is shown in Sec. 3, a unit PG box with reasonable resolutions contains particles ranging from a few hundred thousand to a few million, which can be constructed at a low computational cost on a modern desktop machine.

We should also point out a limitation of the PG box-based method: there is an artificial periodic fabric pattern within the model. Since a PG box is used as a representative volume element (RVE) to fill a spatial domain containing the model, any local anisotropy in the PG box is propagated throughout the domain with an artificial periodicity of the size of the rescaled PG boxes. This artificial fabric pattern, e.g., see Fig. 3 (b) and (c) above, becomes more pronounced for coarse PG boxes because more coarse rescaled PG boxes are needed to fill a given space. As already seen in Sec. 3, the specimens made of the coarsest PG boxes (PL4/PF4) showed stress-strain curves that were not consistent with those of the specimens made of finer PG boxes. Although convergence on failure envelope parameters was observed at finer resolutions in this study, it should be noted that a triaxial test was performed under a quasi-static loading. For problems where dynamic properties are critical, such as wave propagation and fracture evolution, the influence of the resolution-dependent artificial fabric patterns should be studied in more detail in the future.

Another limitation of the current PG box-based method is the assumption of homogeneity within the model, which is common in numerical landslide simulations. As mentioned above, a PG box is used

<sup>2</sup> Ranked No. 2 on the Top500 list of supercomputers as of Nov. 2022: <https://www.top500.org/lists/top500/2022/11/>.

as an RVE to fill a spatial domain for modeling. The homogeneity assumption allows a seamless connection of PG boxes to form a homogeneous domain with the same properties as the PG box. However, soils are often inhomogeneous and stratified, especially when considering a large spatial domain. Such inhomogeneity in material properties requires different types of PG boxes to be combined within a slope model. How to account for the material inhomogeneity to construct more accurate models using PG boxes remains a challenging future work.

## 6. Summary

In this study, we proposed a new modeling technique based on periodic granular (PG) boxes to construct large-scale DEM landslide models. An iterative procedure was used to generate PG boxes with controlled volume fraction. The quality of PG boxes was analyzed in terms of fabric and mechanical properties under the influence of resolution (particle-size) and interparticle friction. Using the PG box-based method with the actual slope topology of the Aso Bridge landslide, a slope model composed of 6.5 billion particles with a maximum radius of 5 cm was successfully constructed. In addition, a test simulation was performed on a coarser slope model composed of about 8 million particles with a maximum radius of 0.5 m, which was constructed using the same PG box-based method. The test simulation verified the ability of the slope model to reproduce excavation phenomena during a landslide.

From the quality analysis, we found that the fabrics of the PG boxes made of frictionless particles converged to be isotropic while anisotropy was introduced with the presence of friction. For a unit-length PG box, the resolution level with a particle radius of 0.01 m was found to be fine enough to have a converged distribution of the contact overlaps, indicating a converged packing fabric. The mechanical properties of PG boxes were quantified as the failure envelope parameters, the cohesion, and internal friction, measured from corresponding numerical triaxial tests. While the confining pressure was found to influence the variation of the stress-strain curves, the results were consistent for specimens made of finer PG boxes. For specimens prepared with frictionless particles (SPL#), the relative errors in the measured failure envelope parameters were small, a few percent at most, for PG boxes with finer resolutions. On the other hand, it was found that the peak stress in the stress-strain curves of the specimens prepared under frictional conditions (SPF#) was weakened compared to the strength of the specimens SPL#. The anisotropic fabrics introduced by friction in SPF# are believed to contribute to this weakening.

Accompanying the demonstration of a slope model with billions of particles and the test landslide simulation, the necessity of fine resolution simulations for landslide simulation was briefly analyzed from the perspective of the resolution-dependent errors in impact force evaluation. The efficiency and flexibility of using the PG box-based method for constructing large-scale DEM models were discussed in comparison with the conventional free-fall modeling method. In addition, two limitations of the current PG box-based method, an artificial periodicity and a homogeneity assumption, were pointed out, which require further analysis and improvement and will be pursued as future work.

This study presented a fine-resolution DEM model of an excavatable slope with centimeter-sized particles, the finest ever, and a test landslide simulation on a coarser slope model with at sub-meter resolution. The coarser resolution test stimulation has already demonstrated some verisimilitude of the mass entrainment due to excavation during the sliding process. In addition, the variation in landslide excavation, deposition, and runout distance caused by changes in particle size alone indicates the need for further investigation. Although significant computational resources will be required, simulation results from even finer slope models are promising to provide insights into the scientific understanding of landslides and to provide more accurate impact-force estimates for the design or evaluation of mitigation measures. Thus, this study can be considered a solid step towards the simulation of large-scale landslides with fine resolution.

## CRediT authorship contribution statement

**Jian Chen:** Visualization, Writing – original draft, Writing – review & editing. **Mikito Furuichi:** Conceptualization, Visualization, Writing – original draft, Writing – review & editing. **Daisuke Nishiura:** Visualization, Writing – review & editing.

## Declaration of Competing Interest

The authors declare that they have no known competing financial interests or personal relationships that could have appeared to influence the work reported in this paper.

## Data availability

Data will be made available on request.

## Acknowledgments

We would like to thank Professor M. Asai of Kyushu University for the engaging discussion and sharing of the Aso Bridge landslide data. This study was supported by the Earth Simulator project of the Japan Agency for Marine-Earth Science and Technology (JAMSTEC), and the supercomputer Fugaku provided by RIKEN through the HCPI System Research Project (Project ID:hp210054), a Grant-in-Aid for Scientific Research (JP18K03815, JP19KK0110, JP21K04265) from the Japan Society for the Promotion of Science (JSPS).

## References

- Ali, U., Kikumoto, M., Cui, Y., Gintia, M., Previtali, M., 2023. Role of particle rotation in sheared granular media. *Acta Geotech.* 18, 4599–4614.
- Bao, Y., Huang, Y., Liu, G., Zeng, W., 2020. SPH Simulation of High-Volume Rapid Landslides Triggered by Earthquakes Based on a Unified Constitutive Model. Part II: Solid-Liquid-Like Phase Transition and Flow-Like Landslides. *Int. J. Comput. Methods* 17, 1850149.
- Berzi, D., Jenkins, J., Richard, P., 2020. Extended kinetic theory for granular flow over and within an inclined erodible bed. *J. Fluid Mech.* 885, A27.
- Bonneau, F., Scholtès, L., Rambure, H., 2021. An algorithm for generating mechanically sound sphere packings in geological models. *Comput. Particle Mech.* 8, 201–214.
- Bui, H., Fukagawa, R., Sako, K., Ohno, S., 2008. Lagrangian meshfree particles method (SPH) for large deformation and failure flows of geomaterial using elastic-plastic soil constitutive model. *Int. J. Numer. Anal. Meth. Geomech.* 32, 1537–1570.
- Cabrera, M., & Estrada, N., 2021. Is the grain size distribution a key parameter for explaining the long runout of granular avalanches? *Journal of Geophysical Research: Solid Earth*, Volume 126, e2021JB022589.
- Campello, E., Cassares, K., 2016. Rapid Generation of Particle Packs at High Packing Ratios for DEM Simulations of Granular Compacts. *Latin American J. Solids Struct.* 13, 23–50.
- Chang, C., Yin, Z.-Y., 2010. Micromechanical Modeling for Inherent Anisotropy in Granular Materials. *J. Eng. Mech.* 136, 830–839.
- Chen, J., Furuichi, M., Nishiura, D., 2020. Discrete Element Simulation and Validation of a Mixing Process of Granular Materials. *Materials* 13, 1208.
- Chen, J., Nishiura, D., Furuichi, M., 2021. DEM study of the influences of the geometric and operational factors on the mechanical responses of an underwater mixing process. *Powder Technol.* 392, 251–263.
- Chen, J., Kitamura, A., Barbieri, E., Nishiura, D., Furuichi, M., 2022. Analyzing effects of microscopic material parameters on macroscopic mechanical responses in underwater mixing using discrete element method. *Powder Technol.* 401, 117304.
- Cil, M., Alshibli, K., 2014. 3D analysis of kinematic behavior of granular materials in triaxial testing using DEM with flexible membrane boundary. *Acta Geotech.* 9, 287–298.
- Crosta, G.B., Imposimato, S., Roddeman, D., Chiesa, S., Moia, F., 2005. Small fast-moving flow-like landslides in volcanic deposits: : The 2001 Las Colinas Landslide (El Salvador). *Eng. Geol.* 79, p. 185'214.
- Cui, L., O'ullivan, C., O'neill, S., 2007. An analysis of the triaxial apparatus using a mixed boundary three-dimensional discrete element model. *Géotechnique*, Volume 57, pp. 831-844.
- Cundall, P., Strack, O., 1979. A discrete numerical model for granular assemblies. *Géotechnique* 29, 47–65.
- Cundall, P.A., 1988. Computer Simulations of Dense Sphere Assemblies, In: *Studies in Applied Mechanics*, Editor(s): Masao Satake, James T. Jenkins, Volume 20, pp. 113–123.
- Dai, F., Wang, F.W., Huang, Y., Song, K., Ito, A., 2016. SPH-based numerical modeling for the post-failure behavior of the landslides triggered by the 2016 Kumamoto earthquake. *Geoenvironmental Disasters* 3, 24.

- Dang, K., Sassa, K., Fukuoka, H., Sakai, N., Sato, Y., Takara, K., Quang, L.H., Loi, D.H., Tien, P.V., Ha, N.D., 2016. Mechanism of two rapid and long-runout landslides in the 16 April 2016 Kumamoto earthquake using a ring-shear apparatus and computer simulation (LS-RAPID). *Landslides* 13, 1525–1534.
- Dilley, R., et al., 2005. Natural disaster hotspots: A global risk analysis. World Bank Group, Washington, D.C.
- Doi, I., Kamai, T., Azuma, R., Wang, G.H., 2019. A landslide induced by the 2016 Kumamoto Earthquake adjacent to tectonic displacement - Generation mechanism and long-term monitoring. *Eng. Geol.* 248, 80–88.
- Duncan, J., Wright, S., 2005. *Soil Strength and Slope Stability*. John Wiley & Sons, Hoboken(N.J).
- Furuichi, M., Chen, J., Nishiura, D., Arai, R., Yamamoto, Y., 2023. Thrust formation using a numerical granular rock box experiment. *Tectonophysics*, Volume 862, 229963.
- Furuichi, M., Nishiura, D., 2017. Iterative load-balancing method with multigrid level relaxation for particle simulation with short-range interactions. *Comput. Phys. Commun.* 219, 135–148.
- Furuichi, M., Nishiura, D., Asai, M., Hori, T., 2017. The first real-scale DEM simulation of a sandbox experiment using 2.4 billion particles. The International Conference for High Performance Computing, Networking, Storage and Analysis SC2017.
- Furuichi, M., Nishiura, D., Kuwano, O., Baulville, A., Hori, T., Sakaguchi, H., 2018. Arcuate stress state in accretionary prisms from real-scale numerical sandbox experiments. *Sci. Rep.* 8, 8685.
- Guo, N., Zhao, J.D., 2013. The signature of shear-induced anisotropy in granular media. *Comput. Geotech.* 47, 1–15.
- Hertz, H., 1881. Ueber die Berührung fester elastischer Körper. *Journal für die reine und angewandte Mathematik* 92, 156–171.
- Highland, L. & Bobrowsky, P., 2008. The Lan-slide Handbook - A Guide to Understanding Landslides. In: *Geological Survey Circular* 1325. Reston, Virginia, U.S.: US Geological Survey.
- Huang, Y., Dai, Z., Zhang, W., Chen, Z., 2011. Visual simulation of landslide fluidized movement based on smoothed particle hydrodynamics. *Nat. Hazards* 59, 1225–1238.
- Hung, C., Liu, C.-H., Lin, G.-W., Leshchinsky, B., 2019. The Aso-Bridge coseismic landslide: a numerical investigation of failure and runout behavior using finite and discrete element methods. *Bull. Eng. Geol. Environ.* 78, 2459–2472.
- Iverson, R., et al., 2011. Positive feedback and momentum growth during debris-flow entrainment of wet bed sediment. *Nat. Geosci.* 4, 116–121.
- Iverson, R., Ouyang, C., 2015. Entrainment of bed material by Earth-surface mass flows: Review and reformulation of depth-integrated theory. *Rev. Geophys.* 53, 27–58.
- Jerier, J.-F., et al., 2011. Study of cold powder compaction by using the discrete element method. *Powder Technol.* 208, 537–541.
- Jerier, J.-F., Richefeu, V., Imbault, D., Donzé, F.-V., 2010. Packing spherical discrete elements for large scale simulations. *Comput. Methods Appl. Mech. Eng.* 199, 1668–1676.
- Jibson, R.W., 2011. Methods for assessing the stability of slopes during earthquakes - A retrospective. *Eng. Geol.* 122, 43–50.
- JSECE, 2016. Investigation report on the landslide disasters caused by the 2016 Kumamoto earthquake (free translation from Japanese). Jpn Soc. Eros. Control Eng. URL:[http://www.jsece.or.jp/archive/survey/20160421/20161213\\_workshop.pdf](http://www.jsece.or.jp/archive/survey/20160421/20161213_workshop.pdf).
- Kawamoto, R., Ando, E., Viggiani, G., Andrade, J., 2018. All you need is shape: Predicting shear banding in sand with LS-DEM. *J. Mech. Phys. Solids* 111, 375–392.
- Krengel, D., Chen, J., Kikumoto, M., 2023. Effects of particle angularity on the bulk-characteristics of granular assemblies under plane strain condition. *Comput. Geotech.* 164, 105812.
- Lai, Z., Vallejo, L.E., Zhou, W., Ma, G., Espitia, J.M., Caicedo, B., Chang, X., 2017. Collapse of granular columns with fractal particle size distribution: Implications for understanding the role of small particles in granular flows. *Geophys. Res. Lett.* 44, 12181–12189.
- Lai, Q., Zhao, J., Huang, R., Wang, D., Ju, N., Li, Q., Wang, Y., Xu, Q., Zhao, W., 2022. Formation mechanism and evolution process of the Chada rock avalanche in Southeast Tibet, China. *Landslides* 19, 331–349.
- Liu, G., Thompson, K., 2000. Influence of computational domain boundaries on internal structure in low-porosity sphere packings. *Powder Technol.* 113, 185–196.
- Liu, W., Wang, D., Zhou, J., He, S., 2019. Simulating the Xinmo landslide runout considering entrainment effect. *Environ. Earth Sci.* 78, 585.
- Matuttis, H.-G., Chen, J., 2014. Understanding the discrete element method: simulation of non-spherical particles for granular and multi-body systems. John Wiley & Sons, s. 1.
- Mindlin, R., 1949. Compliance of Elastic Bodies in Contact. *J. Appl. Mech.* 16, 259–268.
- Morikawa, D.S., Asai, M., 2022. A phase-change approach to landslide simulations: Coupling finite strain elastoplastic TLSPh with non-Newtonian IISPh. *Comput. Geotech.* 148, 104815.
- Mreyen, A.-S., Donati, D., Elmo, D., Donze, F.V., Havenith, H.-B., 2022. Dynamic numerical modelling of co-seismic landslides using the 3D distinct element method: Insights from the Balta rockslide (Romania). *Eng. Geol.* 307, 106774.
- Nishiura, D., Furuichi, M., & Sakaguchi, H., 2015. Computational performance of a smoothed particle hydrodynamics simulation for shared-memory parallel computing. *Computer Physics Communications*, September, Volume 194, pp. 18–32.
- Nishiura, D., Sakaguchi, H., 2011. Parallel-vector algorithms for particle simulations on shared-memory multiprocessors. *J. Comput. Phys.* 230, 1923–1938.
- Oda, M., 1982. Fabric tensor for discontinuous geological materials. *Soils Found.* 22 (4), 96–108.
- Oger, L., Ippolito, I., Vidales, A.M., 2007. How disorder can diminish avalanche risks: effect of size distribution, Precursor of avalanches. *Granular Matter* 9, 267–278.
- Peng, W., et al., 2019. Forecasting Landslides via Three-Dimensional Discrete Element Modeling: Helong Landslide Case Study. *Appl. Sci.* 9, 5242.
- Pudasaini, S.P., Krautblatter, M., 2021. The mechanics of landslide mobility with erosion. *Nat. Commun.* 12, 6793.
- Putra, O., et al., 2020. Shear strength characteristic of unsaturated undisturbed black volcanic ash soil in Kumamoto under static and cyclic loading. *Lowland Technology International* 22 (2), 280–289.
- Qin, Y., Liu, C., Zhang, X., Wang, X., Shi, B., Wang, Y., Deng, S., 2021. A three-dimensional discrete element model of triaxial tests based on a new flexible membrane boundary. *Sci. Rep.* 11, 4753.
- Rothenburg, L., Bathurst, R., 1989. Analytical study of induced anisotropy in idealized granular materials. *Géotechnique* 39, 601–614.
- Sakaguchi, H., Makinouchi, A., & Muhlhaus, H., 2000. *Three-dimensional particle based modeling of frictional behaviour in shear zones*. In: Proceeding of 2nd ACES (APEC Cooperation for Earthquake Simulation) Workshop, October 16–20, Hakone, Japan (2000).
- Satake M. The role of the characteristic line in static soil behavior. In: Balkema AA, editor. IUTAM symposium on deformation and failure of granular materials, Delft; 1982. p. 63–8.
- Scholtés, L., Donzé, F.-V., 2013. A DEM model for soft and hard rocks: Role of grain interlocking on strength. *J. Mech. Phys. Solids* 61, 352–369.
- Soga, K., Alonso, E., Yerro, A., Kumar, K., Bandara, S., 2016. Trends in large-deformation analysis of landslide mass movements with particular emphasis on the material point method. *Géotechnique* 66, 248–273.
- Song, K., Wang, F., Dai, Z., Ito, A., Osaka, O., Sakata, S., 2019. Geological characteristics of landslides triggered by the 2016 Kumamoto earthquake in Mt. Aso volcano, Japan. *Bull. Eng. Geol. Environ.* 78, 167–176.
- Thornton, C., 2000. Numerical simulations of deviatoric shear deformation of granular media. *Géotechnique* 50, 43–53.
- Tiwari, B., Marui, H., 2000. Residual Shear Strength Properties of the Soil from Landslide Area, Using Ring Shear Test. *Ann. Rep. Saigai-ken, Niigata Univ.* No.22, 31–43.
- Troncone, A., Pugliese, L., Conte, E., 2022. Analysis of an excavation-induced landslide in stiff clay using the material point method. *Eng. Geol.* 296, 106479.
- Visscher, W., Bolsterli, M., 1972. Random Packing of Equal and Unequal Spheres in Two and Three Dimensions. *Nature* 239, 504–507.
- Wang, F., Sassa, K., 2010. Landslide simulation by a geotechnical model combined with a model for apparent friction change. *Phys. Chem. Earth* 35, 149–161.
- Wasowski, J., Keefer, D., Lee, C.-T., 2011. Toward the next generation of research on earthquake-induced landslides: Current issues and future challenges. *Eng. Geol.* 122, 1–8.
- Yang, H., Xu, W.-J., Sun, Q.-C., Feng, Y., 2017. Study on the meso-structure development in direct shear tests of a granular material. *Powder Technol.* 314, 129–139.
- Yang, W., Zhou, Z., Pinson, D., Yu, A., 2014. Periodic Boundary Conditions for Discrete Element Method Simulation of Particle Flow in Cylindrical Vessels. *Ind. Eng. Chem. Res.* 53, 8245–8256.
- Zhang, B., Huang, Y., 2022. Numerical and analytical analyses of the impact of monodisperse and bidisperse granular flows on a baffle structure. *Landslides* 19, 2629–2651.
- Zhang, B., Huang, Y., Liu, J., 2021. Micro-mechanism and efficiency of baffle structure in deceleration of granular flows. *Acta Geotech.* 16, 3667–3688.
- Zhu, C., Huang, Y., Sun, J., 2023. A granular energy-controlled boundary condition for discrete element simulations of granular flows on erodible surfaces. *Comput. Geotech.* 154, 105115.